



UNIVERSIDAD AUTÓNOMA DE CHIAPAS

FACULTAD DE CIENCIAS EN FÍSICA Y MATEMÁTICAS

CONSTRAINING THE NATURE OF DARK MATTER AND
COSMIC INFLATION USING CMB SPECTRAL
DISTORTIONS

T E S I S

QUE PARA OBTENER EL GRADO DE:

DOCTOR EN CIENCIAS FÍSICAS

PRESENTA:

RAÚL ANTONIO HENRÍQUEZ ORTIZ PS1608

DIRECTOR DE TESIS:

DR. JORGE HIRAM MASTACHE DE LOS SANTOS

CO-DIRECTORA DE TESIS:

DRA. KAREN SALOMÉ CABALLERO MORA

Tuxtla Gutiérrez, Chiapas; febrero de 2023





Tuxtla Gutiérrez, Chiapas
20 de Febrero de 2023
Oficio No. FCFM/0099/23

Dr. Jorge Hiram Mastache de los Santos
Dra. Karen Salomé Caballero Mora
Director de Tesis
Co-Asesora de Tesis
Presente

Por este medio me permito informarle que una vez efectuada la revisión de la tesis denominada:

“CONSTRAINING THE NATURE OF DARK MATTER AND COSMIC INFLATION USING CMB SPECTRAL DISTORTIONS”.

Ha sido aceptado para sustentar el Examen de Grado de Doctorado en Ciencias Físicas del **Mtro. Raúl Antonio Henríquez Ortiz** con matrícula escolar PS1608.

Se autoriza su impresión en virtud de cumplir con los requisitos correspondientes.

Atentamente

“Por la conciencia de la necesidad de servir”

DIRECCIÓN
FCFM

Dra. Karen Salomé Caballero Mora
Directora

C.c.p. Dr. Florencio Corona Vázquez, Secretario Académico de la FCFM.
CP. Juan Manuel Aguiar Gámez.- Encargado de Posgrado FCFM
Archivo / Minutario
KSCM /jmag



Código: FO-113-09-05

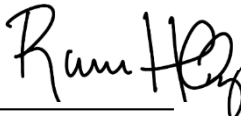
Revisión: 0

CARTA DE AUTORIZACIÓN PARA LA PUBLICACIÓN ELECTRÓNICA DE LA TESIS DE TÍTULO Y/O GRADO.

El suscrito Raúl Antonio Henríquez Ortiz, autor de la tesis bajo el título de “Constraining the nature of dark matter and cosmic inflation using CMB spectral distortions,” presentada y aprobada en el año 2023 como requisito para obtener el grado de Doctor en Ciencias Físicas, autorizo a la Dirección del Sistema de Bibliotecas Universidad Autónoma de Chiapas (SIBI-UNACH), a que realice la difusión de la creación intelectual mencionada, con fines académicos para que contribuya a la divulgación del conocimiento científico, tecnológico y de innovación que se produce en la Universidad, mediante la visibilidad de su contenido de la siguiente manera:

- Consulta del trabajo de título o de grado a través de la Biblioteca Digital de Tesis (BIDITE) del Sistema de Bibliotecas de la Universidad Autónoma de Chiapas (SIBI-UNACH) que incluye tesis de pregrado de todos los programas educativos de la Universidad, así como de los posgrados no registrados ni reconocidos en el Programa Nacional de Posgrados de Calidad del CONACYT.
- En el caso de tratarse de tesis de maestría y/o doctorado de programas educativos que sí se encuentren registrados y reconocidos en el Programa Nacional de Posgrados de Calidad (PNPC) del Consejo Nacional de Ciencia y Tecnología (CONACYT), podrán consultarse en el Repositorio Institucional de la Universidad Autónoma de Chiapas (RIUNACH).

Tuxtla Gutiérrez, Chiapas; a los 20 días del mes de febrero del año 2023.

Raúl Antonio Henríquez Ortiz 
Nombre y firma del Tesista o Tesistas

Acknowledgments

First of all I would like to thank my supervisor Dr. Jorge Mastache for all help towards finishing my degree and continuing my research career. Thank you for your patience, for your confidence in me and for your continuing support. Also, special thanks to Dra. Karen Caballero for all guidance, support and help during my PhD. I am also grateful to Dr. Saul Ramos for the tremendous help that provided for the completion in a part of this research.

I would like to extend my sincere thanks to professors: Dr. Claudio Contreras, Dr. Aldo Aparicio, Dr. Pavel Castro, and Dr. Roberto Arceo, for the help and support in different moments throughout my PhD.

Words cannot express my gratitude to my wife, Jennifer Aguilar, for all support, compassion and love during this four year ago. I also dedicate this work to my parents, my brother and sister and all me family, who helped me in many moments of difficulty during this time of studies.

Finally, none of this work would have been possible without the financial support from Universidad de El Salvador, Universidad Autónoma de Chiapas and Instituto de Capacitación y Vinculación Tecnológica del Estado de Chiapas.

Contents

1	Introduction	13
1.1	Motivation	13
1.2	Organization of this thesis	15
2	Cosmological background	17
2.1	Friedmann Robertson Walker model	17
2.2	The Cosmic Microwave Background Radiation	23
2.3	Dark matter	25
2.3.1	Missing Satellites	26
2.3.2	The cusp-core problem	26
2.4	Inflation scenario	27
2.4.1	Horizon problem	28
2.4.2	Flatness problem	30
2.4.3	The physics of inflation	31
2.4.4	Inflation as scalar field dynamics	31
2.4.5	Slow-roll approximation	33
2.4.6	Initial conditions	35
2.4.7	Power spectrum of primordial curvature perturbations	36
3	Thermalization and Spectral distortions	39
3.1	The Boltzmann equation	39
3.2	Thermalization of CMB spectral distortions	41
3.2.1	Evolution of the photons in the Universe	41

3.3	Analytic descriptions for μ and y distortion	44
3.3.1	The μ -spectral distortion	45
3.3.2	The y -spectral distortion	45
4	Spectral distortions from dark sector	47
4.1	QCD dark matter scenario	47
4.2	Decaying dark particle scenario	51
4.3	Spectral distortions from QCD dark matter	54
5	Spectral distortions from inflation	57
5.1	Axion monodromy model	57
5.2	Damping of primordial small-scale perturbations	60
5.3	Spectral distortions from axion monodromy	62
5.4	Planck constraints on n_s and r	67
6	Summary and Conclusions	71
	Appendices	81
A.1	The visible function $\mathcal{J}_\mu(z)$ and $\mathcal{J}_y(z)$	83
B.2	Analytic exact form of δn_s	84
C.3	The k -space window	85

List of Figures

2.1	Evolution of the energy densities of the Universe's main constituents	23
2.2	The CMB frequency spectrum	24
2.3	Prediction with Λ CDM of Milky Way satellite galaxies	27
2.4	Predict of the dark matter halos profile	28
2.5	Illustration of the horizon problems	30
4.1	Likelihoods for parameters on the BDM model	49
4.2	Function dQ/dz for $a_c = 5 \times 10^{-7}$ and $a_c = 1.99 \times 10^{-7}$	52
4.3	Function dQ/dz varying Γ_χ for $v_c = 0.01$ and $v_c = 0.71$	53
4.4	v_c -dependence of $\Gamma_\chi/\Gamma_{\text{crit}}$ on μ and y SD, for our benchmark choices of a_c . .	55
4.5	Σ_χ -dependence of $\Gamma_\chi/\Gamma_{\text{crit}}$ on μ and y SD	56
4.6	Predictions on the contribution to the distortion ΔI of the photon intensity arising from μ and y SD, in the QCD dark scenario	56
5.1	Constraints at 68% C.L. for the axion decay constant f_0 and the modulating parameter b for $p = 4/3$ based on Planck's data	62
5.2	μ and y SD in axion-monodromy inflation in the (b, f_0) parameter space . . .	63
5.3	p_f -dependence of μ and y SD in models based on axion monodromy for our benchmark choices of p	65
5.4	Values of μ and y SD as functions of the axion decay constant f_0 and the frequency drift p_f in inflationary models based on axion monodromy	66
5.5	Predictions on the contribution to the distortion ΔI of the photon intensity arising from μ and y SD in axion monodromy inflationary models	68

5.6	Predictions for n_s and r from axion monodromy inflation, with $50 \leq N_* \leq 60$ e-folds contrasted against the observational constraints from the CMB Planck data in combination with baryon acoustic oscillation (BAO), CMB lensing data and BICEP/Keck data	70
1	The visible function for μ and y SD in the redshift range $2 \times 10^6 \lesssim z \lesssim 10^3$.	83
2	Comparison between the approximation and exact analytic function of δn_s in the range $10^{-5} \lesssim f_0 \lesssim 10^{-1}$	84
3	The k -space window function for μ and y SD in the wave number range $10^{-2} \lesssim k \lesssim 10^4$	85

List of Tables

- 2.1 Observational values of cosmology parameters 21
- 2.2 Main epoch in the formation of the CMB 24
- 4.1 Parameters for our choices computed for $\Sigma_\chi, \Gamma_\chi, v_c$ and a_c 54
- 5.1 Approximate values of some parameters for our benchmark choices of p in
inflationary models based on axion monodromy 60
- 5.2 Dominant predicted values of μ and y SD by inflationary models with axion
monodromy for a choice monomial powers p and fixed $p_f = -0.7$ 64
- 5.3 Comparison between the maximal values of SD in axion monodromy (with
 $b = 0.01$) and power-law inflationary models ($b = 0$) 66
- 5.4 Improved parameters of axion-monodromy inflation with fixed values of $b =$
 $f_0 = 0.01, p_f = -0.7, k_\star = 0.05 \text{ Mpc}^{-1}$ and $N_\star = 57.5$ 68

Abstract

With the advent of new missions to probe spectral distortions of the cosmic microwave background with unprecedented precision, the study of theoretical predictions of these signals becomes a promising avenue to test our description of the early Universe.

To explore new constraints on dark matter and inflation based on alternative models beyond to cosmological standard model, we compute the spectral distortions of two models, revealing interesting features that maybe compatible with Planck data and future missions like the Primordial Inflation Explorer (PIXIE). First, for the dark matter model we used a QCD dark matter scenario that is a model characterized by a phase transition in the early universe. Second, for the inflation model we used the axion monodromy, whose main feature is a potential with oscillations.

In the QCD dark matter scenario we compute μ and y distortions from values of the free parameters of the model, the magnitude of the spectral distortions are within the range of PIXIE. On the other hand, the framework of axion monodromy, the predicted distortions are up to 10% larger than the signals obtained from the fiducial Λ CDM model and distinguishable. However, contrasting with the predictions of the simplest power-law inflationary potentials challenges the falsifiability of axion monodromy as it would require to reduce at least 100 times the current forecast error of the PIXIE satellite, which should be possible in some surveys setups. Both models show interesting results that could be measurable in the future.

Notation and Conventions

Throughout this thesis, we have systematically used the metric convention $(-+++)$, and we follow the convention of [1]. In the Minkowski limit, it corresponds to

$$\eta_{\mu\nu} = \text{diag}(-1, 1, 1, 1), \quad (1)$$

and we use Einstein's summation convention where repeated indices are summed over. We use Greek letters for spacetimes indices, $\mu = 0, 1, 2, 3$, and Latin letters for spatial indices, $i = 1, 2, 3$. Spatial vectors are denoted by \mathbf{x} and their components by x^i with magnitudes $x = |\mathbf{x}|$. For to raise and lower indices on four-vectors (and on general tensors), we used

$$A_\mu = g_{\mu\nu}A^\nu \quad \text{and} \quad A^\mu = g^{\mu\nu}A_\nu, \quad (2)$$

where $g^{\mu\nu}$ is the inverse metric defined by

$$g^{\mu\lambda}g_{\lambda\mu} = \delta_\nu^\mu = \begin{pmatrix} 1, & \mu = \nu \\ 0, & \mu \neq \nu \end{pmatrix}.$$

Derivatives with respect to physical time t are denoted as $df/dt = \dot{f}$ and with respect to conformal time η are given by $df/d\eta = a\dot{f}$, where $a = a(t)$ is the scale factor. We work in natural units, for which

$$G = \hbar = c = 1, \quad (3)$$

and in chapter 2 and 5, we work in units where reduce Planck mass is $M_{\text{pl}} = m_{\text{pl}}/\sqrt{8\pi} = 1$. Where m_{pl} is the 4-th dimensional Planck mass.

Chapter 1

Introduction

1.1 Motivation

In the last decade has been an exponential increase in obtaining high-precision from cosmological observations. It has also been a considerable increase in the number of techniques available to probe and validate such data. This has contributed to being able to establish the standard model of cosmology. Observations of the Universe, such as type Ia supernovae and Cosmic Microwave Background (CMB) radiation have shown that the Universe: is spatially flat, homogeneous and isotropic on large scales, that the 70% of the Universe and driving its accelerated expansion, and the 26% of the Universe is composed of a massive enough to clustering surrounding to the baryonic matter at the large scales. The Λ as dark energy, the DM, along with the baryons (filling the remaining 4% of the Universe) are components of the Λ CDM model, which has been consolidated at different scales and regimes, such as the CMB [2; 3; 4], galaxy and quasar surveys [5; 6; 7; 8; 9], lensing probes [10] and supernovae catalogs [11]. Despite its success, the Λ CDM model has fundamental caveats explaining the nature of dark matter and dark energy. Several observations are consistent with the predictions of the standard cosmological model, Λ CDM. However, three main caveats are present within the model. First, it predicts steeply cusped profiles for the dark matter distribution in galaxies [12], the number of small satellite galaxies appears to be fewer than predictions, this problem is called missing satellites [13; 14; 15]. Third, there is a tension between local and cosmolog-

ical determinations of the Hubble constant H_0 [4; 5; 6; 7; 8; 9; 11]. It was just recently that some of this cosmological problem have been approached by spectral distortions (SD) [16].

In the early Universe, photons and baryons are tightly coupled, behaving as a single viscous fluid close to thermal equilibrium due to Compton scattering, Bremsstrahlung scattering, and double Compton scattering, processes that isotropize the photon-baryon fluid. However, early energy injection to the baryon-photon fluid can disrupt thermal equilibrium, causing the CMB to experience small departures from the blackbody distribution. These deviations are known as SD and are sensitive to any energy injection to the CMB at early epochs. CMB SD complement the anisotropy CMB observations and provide a new benchmark to test standard and non-standard cosmological scenarios at small scales. One mechanism in the canonical cosmological model that injects energy is Silk damping [17], which damps acoustic waves smaller than the sound horizon after the perturbation enters the horizon. Through this process, the energy stored at small scales in the radiation fluid is redistributed to larger scales resulting in SD [16; 18; 19; 20; 21]. The thermal diffusion mechanism results in an increase in the average photon temperature. The emerging SD are the mixture of blackbody spectra from regions with different temperatures [22; 23], and their amplitude is proportional to the square of the average temperature perturbations in the photon field [18; 24; 25]. The damping of modes over the wavenumber interval $50 \text{ Mpc}^{-1} \lesssim k \lesssim 10^4 \text{ Mpc}^{-1}$ (equivalent to redshifts $5 \times 10^4 \lesssim z \lesssim 2 \times 10^6$) dissipate their energy while creating a non-zero chemical potential creating μ SD, and the damping modes with $k < 50 \text{ Mpc}^{-1}$ ($z \lesssim 10^4$) results in a so-called y SD, also related to the (thermal and kinematic) Sunyaev-Zeldovich (SZ) effect [24]. Many other standard processes can also contribute to produce SD: the radiation during reionization, supernova feedback and structure formation shocks heat the intergalactic medium at $z \lesssim 10$, leading to a partial up-scattering of CMB photons, causing y SD. Adiabatic cooling of ordinary matter continuously extracts energy from CMB photon bath leading to another small SD depends on baryon density and helium abundance. The recombination process is associated with the emission of photons in free-bound and bound-bound transitions of hydrogen and helium, this causes a small distortion of the CMB [16; 20; 26; 27; 28; 29; 30]. Various non-standard mechanisms induce SD, such as decay and annihilation of relic particles, evaporation of primordial

black holes, primordial magnetic fields, and cosmic strings, see e.g. [31; 32; 33; 34].

The SD were tightly constrained in 1996 by COBE/FIRAS to $|\mu| \leq 9 \times 10^{-5}$ and $|y| \leq 1.5 \times 10^{-5}$ (95% C.L.) [35]. Since models predict typically smaller SD, greater experimental precision had to be awaited to resume research on SD. Fortunately, new experimental missions, such as PIXIE and its enhanced version Super-PIXIE will soon explore SD with expected standard errors $\sigma(\mu) \simeq 3 \times 10^{-8}$, $\sigma(y) \simeq 3.4 \times 10^{-9}$ [36] and $\sigma(\mu) \simeq 7.7 \times 10^{-9}$, $\sigma(y) \simeq 1.6 \times 10^{-9}$ [32; 37], respectively. Moreover, there even exist proposals of alternative configurations of PIXIE with 1000 times improved sensitivity to achieve $\sigma(\mu) = 1.5 \times 10^{-11}$ and $\sigma(y) = 1.2 \times 10^{-12}$ (68% C.L.) [38]. Such sensitivity will be instrumental in falsifying relic decaying dark matter and inflationary models.

In this thesis we are hence driven to provide precise descriptions of the SD features, first we investigated a family of models called QCD dark matter, where unstable dark particles are created, i.e. dark meson, that decay after the confinement scale and deposit a fraction of their energy, into the Standard Model (SM) photons through a coupling of the SM and the dark sector, we calculated the SD signal produced for this mechanism. In the second work, we explored new constraints on inflationary models based on axion monodromy while aiming at falsifying this scenario, we compute the spectral distortions predicted by this model.

1.2 Organization of this thesis

We organize this work as follows. In chapter 2 a brief review of the cosmological background is presented, followed in chapter 3 by an overview of theory of thermalization problem and CMB SD. Using these elements, in chapter 4 the SD are computed and the results are discussed for the QCD dark matter, and in chapter 5 the SD for primordial small-scale perturbation from axion monodromy are computed, these last chapters are the main result of our thesis. Finally, in chapter 6 a brief discussion of our results and outlook is given.

Numerical calculations and the respective plots were obtained with the help of routines developed in Python 3. Partial results presented in this thesis have been published in the following paper:

- R. Henriquez-Ortiz, J. Mastache and S. Ramos-Sanchez, *Spectral distortions from axion monodromy inflation*, **JCAP** 08 (2022) 054, [arXiv:2206.07719]

Chapter 2

Cosmological background

2.1 Friedmann Robertson Walker model

On average, in the Universe at large scales, the clumpy distribution of galaxies is homogeneous and isotropic. As a first approximation, the Universe can be assumed to be homogeneous and isotropic, this is known as the Cosmological principle. The current best theory for the description of the Universe at large scales is the general theory of relativity (GR), which provides a description of the gravitational phenomena as a geometric property of the space-time. The curvature in the space-time in GR is described by a fundamental quantity, the metric, which describes the geometry of a manifold in four dimensions, three of space and one of time. The pseudo-distance between two points in the space-time ds^2 is given by

$$ds^2 = \sum_{\mu, \nu=0}^3 g_{\mu\nu} dx^\mu dx^\nu = g_{\mu\nu} dx^\mu dx^\nu, \quad (2.1)$$

where ds is invariant under a change of coordinate system and the path of a light ray is given by $ds = 0$, the indices μ and ν run over 0, 1, 2, 3. The time coordinate is x^0 and x^1 , x^2 and x^3 are the three spatial coordinates; and $g_{\mu\nu}$ is a covariant symmetric tensor named the metric tensor of the space–time geometry of the Universe.

A particle moves in such a way that the integral along its path is stationary

$$\delta \int_{\text{path}} ds = 0, \quad (2.2)$$

from eq.(2.1) into eq.(2.2), is obtained the path of a free particle, which is called a geodesic, can be described by

$$\frac{d^2 x^i}{ds^2} + \Gamma_{kl}^i \frac{ds^k}{dt} \frac{ds^l}{dt} = 0, \quad (2.3)$$

where the Christoffel symbols are

$$\Gamma_{kl}^i = \frac{1}{2} g^{im} \left[\frac{\partial g_{mk}}{\partial x^l} + \frac{\partial g_{ml}}{\partial x^k} - \frac{\partial g_{kl}}{\partial x^m} \right], \quad (2.4)$$

and

$$g^{im} g_{mk} = \delta_k^i, \quad (2.5)$$

where δ_k^i is the Kronecker delta, which, if $i = k$, is unity and otherwise zero. In GR all equations are tensor equations. A general tensor is a quantity which transforms as follows when coordinates are changed from x^i to x'^i

$$A'^{kl\dots} = \frac{\partial x'^k}{\partial x^m} \frac{\partial x'^l}{\partial x^n} \dots \frac{\partial x^r}{\partial x'^p} \frac{\partial x^s}{\partial x'^q} \dots A_{rs\dots}. \quad (2.6)$$

The upper indices are contravariant and the lower are covariant. In GR the energy-momentum tensor $T_{\mu\nu}$ describes the matter distribution, we can write in tensorial formulation the equivalence of conservation laws of mass, energy, and momentum

$$\frac{\partial T_{\mu\nu}}{\partial x^\nu} = 0, \quad (2.7)$$

e.g. in a perfect fluid approximation, the energy-momentum tensor is

$$T_{\mu\nu} = (\rho + P) U_\mu U_\nu - P g_{\mu\nu}, \quad (2.8)$$

where ρ and P are the energy density and the pressure in the rest frame of the fluid, and U_μ and U_ν are the fluid four-velocity relative to a comoving observer. The properties of curved spaces are codified in the Riemann curvature tensor through the Christoffel symbols

$$R^i_{klm} = \frac{\partial \Gamma^i_{km}}{\partial x^l} - \frac{\partial \Gamma^i_{kl}}{\partial x^m} + \Gamma^i_{nl} \Gamma^n_{km} - \Gamma^i_{nm} \Gamma^n_{kl}. \quad (2.9)$$

From the Riemann tensor, one can form the Ricci tensor

$$R_{ik} = R^l_{ilk}, \quad (2.10)$$

is the Ricci scalar that defines the scalar curvature R as

$$R = g^{ik}R_{ik}. \quad (2.11)$$

From eq.(2.10) and eq.(2.11), we can introduce the cosmological constant Λ , the Einstein tensor is defined

$$G_{\mu\nu} \equiv R_{\mu\nu} - \frac{1}{2}g_{\mu\nu}R - \Lambda g_{\mu\nu} = 8\pi T_{\mu\nu}. \quad (2.12)$$

The eq.(2.12) relates the Einstein tensor $G_{\mu\nu}$ to the energy-momentum tensor $T_{\mu\nu}$. To describing our Universe in a good approximation we need a manifold at any given time, that fulfills the cosmological principle. The Friedmann Robertson Walker (FRW) metric, for an expanding Universe, is the most general space-time metric describing a Universe in which the cosmological principle is fulfilled [39]

$$g_{\mu\nu} = \begin{pmatrix} -1 & 0 & 0 & 0 \\ 0 & a^2(t) & 0 & 0 \\ 0 & 0 & a^2(t) & 0 \\ 0 & 0 & 0 & a^2(t) \end{pmatrix}. \quad (2.13)$$

Where $a(t)$ is the scale factor. For a homogeneous and isotropic perfect fluid with rest-mass energy density ρ and pressure P , the stress–energy tensor has the form

$$T^{\mu}_{\nu} = g^{\mu\lambda}T_{\lambda\nu} = \begin{pmatrix} -\rho(t) & 0 & 0 & 0 \\ 0 & P(t) & 0 & 0 \\ 0 & 0 & P(t) & 0 \\ 0 & 0 & 0 & P(t) \end{pmatrix}. \quad (2.14)$$

The solutions of the eq.(2.12) with the FRW metric eq.(2.13) and eq.(2.14) are the Friedmann

cosmological equations

$$H^2 = \frac{8\pi}{3}\rho - \frac{k}{a^2}, \quad (2.15a)$$

$$\frac{\ddot{a}}{a} = -\frac{4\pi}{3}(\rho + 3P), \quad (2.15b)$$

where k is the curvature parameter, $H(t) = \dot{a}/a$ is the Hubble parameter. A combination of eqs.(2.15) can be rewritten only in term of H , ρ y P . This equation describes energy conservation in the cosmological context

$$\dot{\rho} = -3H(\rho + P), \quad (2.16)$$

eq.(2.16) also could be gotten from the covariant derivative of $T_{\mu\nu}$. All cosmological parameters evaluated today are denoted with subindex 0, for instance, from eq.(2.15) for $k = 0$, we have

$$H^2(t=0) = H_0^2 = \frac{8\pi}{3}\rho_0 = \frac{8\pi}{3}\rho_{\text{crit},0}, \quad (2.17)$$

where ρ_0 is the sum from all contributions to the energy density in the Universe at the present time, $\rho_{\text{crit},0} \equiv 3H_0^2/8\pi$ is the critical density, and indicates the mean density of matter that is required for gravity to halt the expansion of the Universe, and H_0 is the Hubble parameter today (Hubble constant). The densities of the i th component is normalized with $\rho_{\text{crit},0}$

$$\Omega_{i,0} = \frac{\rho_{i,0}}{\rho_{\text{crit},0}}. \quad (2.18)$$

If the curvature term is taken as $k \neq 0$, we can define the curvature energy density

$$\rho_{k,0} = -\frac{3}{8\pi G} \frac{k}{a_0^2}. \quad (2.19)$$

The Universe is composed of baryonic matter, dark matter, photons, neutrinos, and dark energy. In the standard cosmological model dark matter is considered to be cold, this refers a kind of dark particle that interacting weakly with the standard particles, and the dark energy to be a cosmological constant, therefore, the standard model is Λ CDM model. The Planck mis-

Parameter	Meaning	Value	Cite
$\rho_{\text{crit},0}$	critical density	$(8.62 \pm 0.12) \times 10^{-27} \text{ kg m}^{-3}$	[1]
$\Omega_{\text{r},0}$	radiation parameter	8.99×10^{-5}	[1]
$\Omega_{\gamma,0}$	photon parameter	5.35×10^{-5}	[1]
$\Omega_{\text{v},0}$	neutrinos parameter	< 0.003	[1]
$\Omega_{\text{b},0}h^2$	baryon parameter	0.02242 ± 0.00014	[40]
$\Omega_{\text{m},0}h^2$	matter parameter	0.14240 ± 0.00087	[40]
$\Omega_{\Lambda,0}$	dark energy parameter	0.6889 ± 0.0056	[40]
$\Omega_{\text{k},0}$	spatial curvature	0.001 ± 0.002	[40]

Table 2.1: Observational Values of cosmology parameters, which it has adopted the Λ CDM model with a good fit to the observational data, and these are in agree to the Universe spatially flat with contains radiation, matter, and a cosmological constant. Here the Hubble constant is taken as $H_0 = 67.66 \pm 0.42 \text{ km/s/Mpc}$ and $h = H_0/(100 \text{ km/s/Mpc})$ [40].

sion has provided the observational values for the cosmological parameter Ω (see table 2.1).

The geometry of the space can be closed ($k = 1$), flat ($k = 0$) or open ($k = -1$) depending on value of the density parameter. Nowadays, the Universe is considered to be flat due to the constraints given by the observation on the curvature $\Omega_{\text{k},0}$, that is equivalent to $k \approx 0$, from sum in eq.(2.20)

$$\sum_i \Omega_{i,0} = \Omega_{\text{r},0} + \Omega_{\text{m},0} + \Omega_{\Lambda,0} + \Omega_{\text{k},0} = \Omega_0 + \Omega_{\text{k},0} = 1, \quad (2.20)$$

where $\Omega_0 \equiv \Omega_{\text{r},0} + \Omega_{\text{m},0} + \Omega_{\Lambda,0}$. The energy of the photon evolves in reverse of the scale factor due to the expansion of the Universe. Therefore, it is useful to introduce another variable related to the expansion parameter, which is directly observable from the instruments; this is the redshift z , many of the relevant formulas in cosmology are very simple when are expressed in terms of redshift. For a luminous source, e.g. a distance galaxy, the redshift is defined as

$$z = \frac{\lambda_0 - \lambda_e}{\lambda_e} \quad \text{with} \quad a = \frac{1}{1+z}, \quad (2.21)$$

where λ_0 is the wavelength of the radiation from the source observed at O (which we take as the origin of our coordinate system) at time t_0 and emitted by the source at an earlier time t_e . The relationship between ρ and P is known as the equation of state, where P depends only

on ρ in the case of the perfect fluid. In the early Universe, the different components of the Universe can be treated in a good approximation as a perfect fluid with an equation of state

$$P = w\rho, \quad (2.22)$$

where the parameter w is a constant in the range $0 \leq w \leq 1$. The case with $w = 0$ represents dust (pressureless material), this is a good approximation to the behavior of any non-relativistic fluid. On the other hand, a fluid that is non-degenerate and ultrarelativistic in thermal equilibrium for an equation of state with $w = 1/3$, is the case for a gas of photons or neutrinos. Notice the peculiar case which $w = -1$ in eq.(2.22), is for a perfect fluid equivalent of a cosmological constant [41].

The solutions for $\rho(t)$ for every component as function of the redshift can be gotten from eq.(2.16) assumed an adiabatic expansion of the Universe

$$\rho_m = \rho_{m,0}(1+z)^3, \quad (2.23)$$

for non-relativistic matter, for radiation and relativistic matter

$$\rho_r = \rho_{r,0}(1+z)^4, \quad (2.24)$$

and, for the dark energy density

$$\rho_\Lambda = \rho_{\Lambda,0}. \quad (2.25)$$

where $\rho_{m,0}$, $\rho_{r,0}$ and $\rho_{\Lambda,0}$ are the energy density of matter, radiation and dark energy today, respectively. With a cosmological constant, the total density of the Universe scales is

$$\rho(z) = \rho_{\Lambda 0} + \rho_{m0}(1+z)^3 + \rho_{r0}(1+z)^4, \quad (2.26)$$

or in term of Ω using eq.(2.18)

$$\Omega(z) = \Omega_{\Lambda 0} + \Omega_{m0}(1+z)^3 + \Omega_{r0}(1+z)^4. \quad (2.27)$$

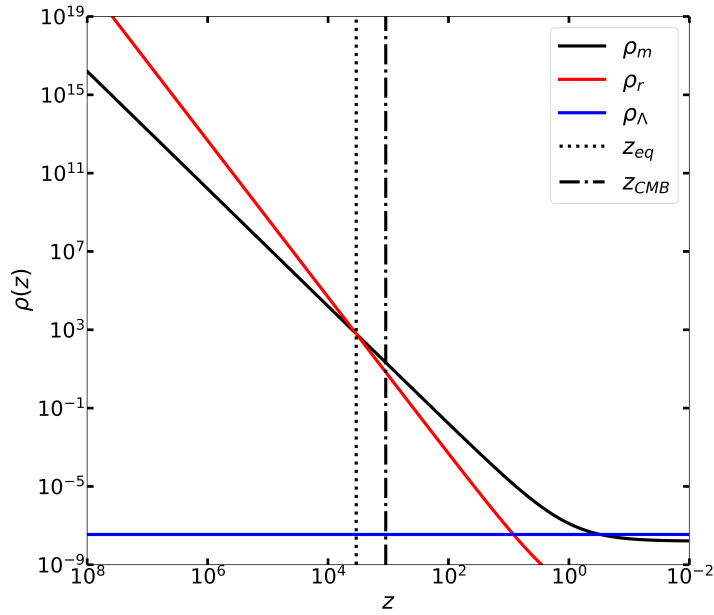


Figure 2.1: Plot showing the evolution of the energy densities of the Universe's main constituents. At high redshift, the radiation dominates (red curve), at middle redshift matter dominates (black curve) and later redshift dark energy is dominating (blue curve). Figure was plotted from data gotten with CLASS code [42]. Here, the values of z_{eq} and z_{CMB} are taken of table 2.2.

Integrating the Friedmann equation, we obtain a relation between time and scale factor

$$H_0 t = \int_0^a \frac{da}{\sqrt{\Omega_{\Lambda,0} + \Omega_{m0} a^{-3} + \Omega_{r0} a^{-4}}}. \quad (2.28)$$

2.2 The Cosmic Microwave Background Radiation

The Big Bang theory of cosmology starts with the idea that the Universe at the beginning was ultra-energetic, smaller than it is today, and the pressure of radiation was the most important component of the energy density. During the radiation epoch, no neutral atoms had yet been formed. Free electrons, protons, and photons with relativistic velocities are the principal component of the Universe. Photons were abundant in the early Universe, they reach thermal equilibrium with a bath of electrons through collisions. As can be see in table 2.2, around a temperature of 0.25 eV, photons decoupled from the matter, and the Universe became trans-

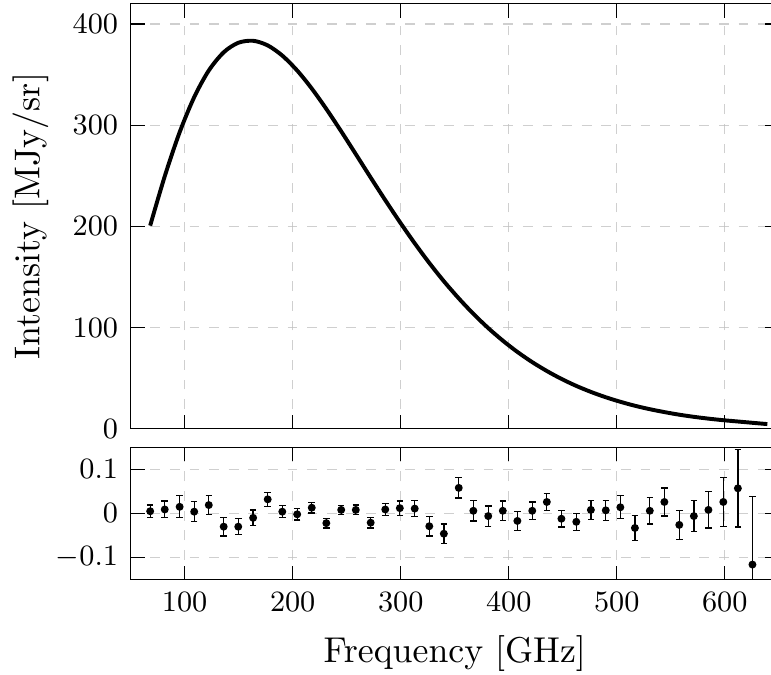


Figure 2.2: CMB frequency spectrum shows a behavior near to blackbody distribution. Figure was gotten from [1].

Event	redshift	temp [eV]	time [y]
Matter-radiation equality	3400	0.81	50000
Recombination	1300	0.30	250000
Photon decoupling	1100	0.25	380000
Last-scattering	1100	0.25	380000

Table 2.2: Main epoch in the formation of the cosmic microwave background. Values extracted from [1].

parent. Nowadays, these photons are observed as the CMB [1].

In the CMB, photons show a stable energy spectrum, as a consequence of the thermal equilibrium of photons, it can be described as a blackbody spectrum, with the temperature $T_0 = 2.7260 \pm 0.0013$ K [40], the fluctuation of CMB temperature is small, $\Delta T/T \sim 10^{-5}$ [39], and contains an enormous amount of information about the composition of our Universe. Systems in equilibrium are characterized by a time-independent distribution function: the Fermi-Dirac distribution (for fermions) or the Bose-Einstein distribution (for bosons)

$$f(p,T) = \frac{1}{e^{(E(p)-\mu)/T} \pm 1}, \quad (2.29)$$

where p is the momentum, μ the chemical potential and T the temperature of the system. The

+ sign is for fermions (e.g. electrons) and – sign for bosons (e.g. photons). Using the proper units in eq.(2.29) for photons with $E = h\nu$ and $T = T_0$, it is plotted the curve in figure 2.2.

From distributions can get the number and energy density

$$n = \frac{g}{(2\pi)^3} \int d^3p f(p, T) = \frac{\zeta(3)}{\pi^2} g T^3, \quad (2.30a)$$

$$\rho = \frac{g}{(2\pi)^3} \int d^3p f(p, T) E(p) = \frac{\pi^2}{30} g T^4, \quad (2.30b)$$

where $E = \sqrt{m^2 + p^2}$ is the energy and g are the degrees of freedom of particle. Using the observed temperature of the CMB, $T_0 \approx 2.73$, it can find the number and energy density of relic photons today

$$n_{\gamma,0} = 2 \frac{\zeta(3)}{\pi^2} g T_0^3 \approx 410 \text{ photons } cm^{-3}, \quad (2.31a)$$

$$\rho_{\gamma,0} = \frac{\pi^2}{15} g T_0^4 \approx 4.6 \times 10^{-34} \text{ gr } cm^{-3}. \quad (2.31b)$$

Where has been used for photons $g = 2$ [39].

2.3 Dark matter

Dark matter represents an outstanding problem in both cosmology and particle physics. From the context of particle physics, dark matter can be made of one or several new particles, which are expected to be electrically neutral, uncolored, weakly-interacting, and stable [43]. The cosmological density of dark matter $\Omega_{\text{dm},0}$ could be inferred from table 2.1

$$\Omega_{\text{dm},0} = \Omega_{\text{m},0} - \Omega_{\text{b},0} \approx 0.263. \quad (2.32)$$

The particles of dark matter could arise from theories Beyond the Standard Model (BSM) of particle physics, this has implicated an enormous proliferation of dark matter candidates, which are currently being sought in an impressive array of accelerator, direct, and indirect detection experiments [44]. The most studied mechanism is thermal production, positing that dark matter particles were in chemical and thermodynamical equilibrium with other species

of the standard model of particles at early Universe, until the dark matter annihilation rate dropped below the expansion rate of the Universe, this leads to the models of Weakly Interacting Massive Particles (WIMPs). The other most discussed dark matter model is the based on Supersymmetry (SUSY), among the most studied candidates are: neutralino and gravitino. Many alternative theories have been proposed in a phenomenological way: Kaluza-Klein gravitons, axinos, quintessinos, Fuzzy dark matter (FDM) and other interesting superWIMPs candidates.

According to the dispersion velocity of dark matter particles, they could be classified as hot (HDM), warm (WDM), or cold dark matter (CDM). The CDM has successfully explained large-scale structure formation in the early Universe as well as the abundance of galaxy clusters in the standard Λ CDM model. The theory faces a number of challenges. For example, the number of satellite galaxies around to milky way is smaller than the expected from Λ CDM model (the missing satellite problem). It also predicts steeply cuspy density profiles, causing a large fraction of haloes to survive as substructures inside larger haloes (the cusp-core problem) [45]. The key question is whether a better understanding of baryon physics, dark matter physics, or both will be required to meet these challenges.

2.3.1 Missing Satellites

The observed stellar mass functions of field galaxies and satellite galaxies in the Local Group are much flatter at low masses than predicted by simulations of dark matter halos mass functions in Λ CDM: $dn/dM_* \propto M_*^{\alpha_g}$ with $\alpha_g \simeq -1.5$ (vs. $\alpha \simeq -1.9$ for dark matter) [46]. The problem is more significant for galactic satellites (see the image in figure 2.3.1), where the observations around the Milky Way are much fewer (50 satellite galaxies approximate) than predicted by N body simulations ($\mathcal{O}(10^3)$ satellites galaxies).

2.3.2 The cusp-core problem

The Λ CDM simulations that include only dark matter predict that dark matter halos are fitted using the Navarro-Frenk-White (NFW) profile for the contribution of the dark matter halo, but

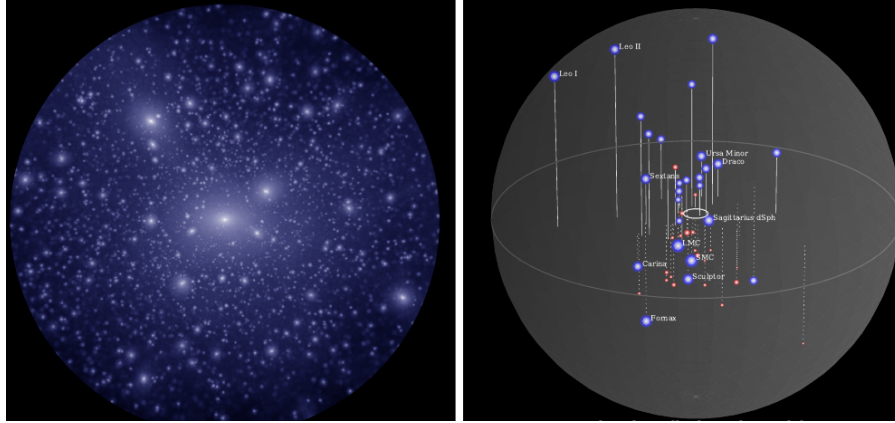


Figure 2.3: The left image shows a N-body simulation with Λ CDM dark matter distribution, within a sphere of radius 250 kpc around the center of Milky Way. The right image shows the current census of Milky Way satellite galaxies (50 satellite galaxies approximate). The galactic disk is represented by the circle inside (15 kpc) and the circle outside has a radius of 250 kpc (with $\mathcal{O}(10^3)$ satellites galaxies). Images were taken from [46].

in the observations, it has been seen that profiles rise steeply at small radii $\rho(r) \propto r^{-\gamma}$, with $\gamma \simeq 0.8 - 1.4$ over the radii of interest for small galaxies [46]. This is in contrast to many low-mass dark matter dominated galaxies with well-measured rotation curves, which prefer fits with a constant density core ($\gamma \approx 0 - 0.5$). In figure 2.3.2, is shown as a dashed line for the typical circular velocity curve predicted for a NFW Λ CDM dark matter halo with $V_{\text{max}} \approx 40 \text{ km s}^{-1}$ compared to the observed rotation curves for two galaxies with the same asymptotic velocity. The observed rotation curves rise much more slowly than the Λ CDM expectation, reflecting core densities that are lower and more core-like than the fiducial prediction.

In recent years, two main ways have been proposed for solving the missing satellite and cusp-core problems. First, the solution through baryon physics. Second, the number of satellite galaxies is suppressed due to the kinematic properties of the dark matter particles [45]. In this thesis, we take the second way by constraining the properties of dark matter particles that influence just the structure formation.

2.4 Inflation scenario

The previous section mentioned that FRW cosmology describes a homogeneous and isotropic Universe, but it was not explained why it is that way. One solution to this problem is to

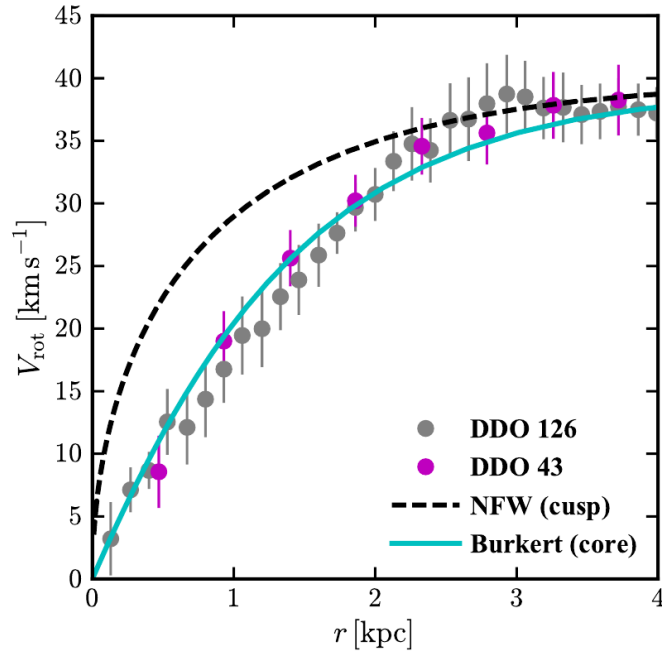


Figure 2.4: The dashed line shows the predict of the dark matter halos profile with NFW for a typical rotation curve $V_{\max} \approx 40 \text{ km s}^{-1}$ galaxy in ΛCDM . This rotation curve rises quickly, reflecting a central density profile that rises as a cusp with $\rho \propto 1/r$. The data points in this figure show the rotation curves of two example galaxies of the size from the LITTLE THINGS survey. Image taken of [46].

assume an early period of accelerated expansion, this period is known as cosmological inflation [47; 48; 49], and refers to the early epoch of exponential expansion of the Universe that sets up the initial conditions of the Hot Big Bang. The inflationary paradigm is well motivated because it provides a solution to some of the problems of the standard cosmological model, such as the horizon and flatness problems (see [50; 51; 52; 53] for some reviews).

2.4.1 Horizon problem

The horizon problem is linked to the grade isotropy in the CMB: how to explain that regions in the CMB sky have the same temperature, whereas their angular separation is too large to correspond to causally connected patches at the time of the last scattering?, at the beginning of the Universe, we have a singularity at the time $t_i \equiv 0$ ($a_i \equiv 0$), and the greatest comoving distance from which an observer at time t will be able to receive signals traveling at the speed

of light is called the comoving horizon or the particle horizon

$$d_h(\eta) = \eta - \eta_i = \int_{t_i}^t \frac{dt}{a(t)} = \int_{\ln a_i}^{\ln a} (aH)^{-1} d \ln a. \quad (2.33)$$

We have seen in the previous section that the early Universe is dominated by radiation. We can write $aT = \text{constant}$, and in a comoving coordinate system, any physical distance grows like

$$d(t) = \frac{T(t_0)}{T(t)} d(t_0). \quad (2.34)$$

Using $T_0 \approx 2.7 \text{ K} \approx 2.3 \times 10^{-13} \text{ GeV}$, the radius of the spherical volume in principle observable today by an observer at the center of the sphere, is $d_{H_0}(t_0) \approx 10^{26} \text{ m}$. At the time of the last scattering t_{LSS} , the radius of the observable Universe is

$$d_{H_0}(t_{LSS}) \approx 7 \times 10^{22} \text{ m}.$$

The maximal distance between of two causally connected points would roughly be

$$d_{H_{LSS}}(t_{LSS}) \approx 2 \times 10^{21} \text{ m}.$$

At last scattering, our observable Universe would therefore have been constituted of about 10^5 causally disconnected regions. But CMB photons emerging from these regions are observed to have all the same temperature, to a 10^{-5} accuracy. At the Planck time, the number of causally disconnected patches would have been much larger, about 10^{89} [54]. As illustration of this problem, we can think in an observer in O at time t_0 (see figure 2.4), $\eta(t_0)$ is the comoving radius of the sphere centered in O separating particles causally connected (region of A' and B') to the observer of particles causally disconnected (region of A and B).

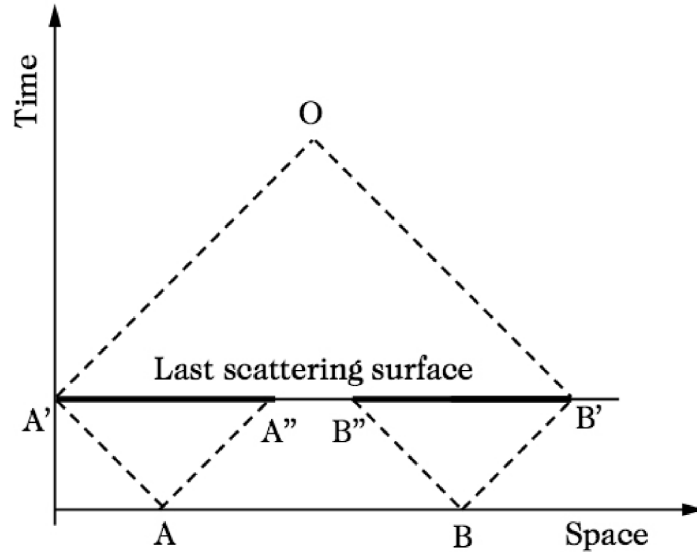


Figure 2.5: Illustration of the horizon problem in standard cosmology. All events that we currently observe are on our past light cone. The CMB is observed from the hypersurface $t = t_0$. The AB' region at last scattering is isothermal in the CMB sky, although it appears to be constituted of causally disconnected patches. Image taken of [54].

2.4.2 Flatness problem

The time-dependent critical density of the Universe could be defined as $\rho_{\text{crit}} = 3m_{\text{pl}}^2 H^2 / 8\pi$. From eq.(2.20) we can write the time-dependent curvature parameter

$$\Omega_k(a) = \frac{\rho_k}{\rho_{\text{crit}}} = \frac{\rho_{\text{crit}} - \rho}{\rho_{\text{crit}}} = \frac{(a_0 H_0)^2}{(aH)^2} \Omega_{k,0}, \quad (2.35)$$

the CMB provides an upper bound on the size of the curvature parameter today, $|\Omega_{k,0}| < 0.005$, and the comoving Hubble radius $(aH)^{-1}$ is growing during the radiation era, but we expect that $|\Omega_{k,0}|$ was smaller in the past than today. For example, roughly at radiation-matter equality we have

$$|\Omega_k(t_{\text{eq}})| \lesssim 3 \times 10^{-6},$$

and at the Planck time,

$$|\Omega_k(t_{\text{pl}})| \lesssim 10^{-60}.$$

Well, if the Universe is not strictly flat, the Λ CDM model does not explain why the spatial curvature is so small [54].

2.4.3 The physics of inflation

The basic condition under such the horizon and flatness problems are solved is an early epoch of accelerated expansion of the Universe. The main feature of inflation is that all physical quantities slowly vary, despite space expanding rapidly [1]. We can see this with a rewrite the change of the time to the comoving Hubble radius as

$$\frac{d}{dt}(aH)^{-1} = -\frac{\dot{a}H + a\dot{H}}{(aH)^2} = -\frac{1}{a}(1 + \varepsilon), \quad (2.36)$$

we define ε as the Hubble slow-roll parameter

$$\varepsilon \equiv -\frac{\dot{H}}{H^2} = -\frac{d \ln H}{dN}, \quad (2.37)$$

and the amount of expansion during inflation is quantified with the parameter number of e-folds N , defined as

$$N \equiv \ln \left[\frac{a}{a_i} \right]. \quad (2.38)$$

Where a_i is the scale factor at the start of inflation. Eq.(2.37) shows that a shrinking of Hubble parameter, $\partial_t(aH)^{-1} < 0$, is associated with $\varepsilon < 1$. It is expected that inflation during a sufficiently time (between 40 and 60 e-folds), which requires that ε remains small for a sufficiently large number of Hubbles times, this condition is quantified with the second Hubble slow-roll parameter [1]

$$\kappa \equiv \frac{d \ln \varepsilon}{dN} = \frac{\dot{\varepsilon}}{H\varepsilon}. \quad (2.39)$$

The fractional change of ε for the condition $|\kappa| < 1$ per e-fold is small.

2.4.4 Inflation as scalar field dynamics

The inflationary epoch is a phase of quasi-exponential accelerated expansion of the Universe, this kind of expansion can be obtained if during inflation, is assumed that the Universe is filled with a scalar field ϕ , called inflaton. Considering a minimally coupled scalar field ϕ with a

Lagrangian density [55]

$$\mathcal{L} = -\frac{1}{2}g^{\mu\nu}\partial_\mu\phi\partial_\nu\phi - V(\phi), \quad (2.40)$$

where $V(\phi)$ is the potential energy density associated to the field. The action of a homogeneous scalar field $\phi \equiv \phi(t)$ in an expanding FRW spacetime is

$$S = \int d^4x \sqrt{-g} \mathcal{L} = \int d^4x \sqrt{-g} \left[-\frac{1}{2}g^{\mu\nu}\partial_\mu\phi\partial_\nu\phi + V(\phi) \right], \quad (2.41)$$

where $g \equiv \det g_{\mu\nu}$ is the determinant of the FLRW metric determinant. In the equation of motion of the scalar field, we perform the variation of the action under the variation of the inverse metric $g^{\mu\nu} \rightarrow g^{\mu\nu} + \delta g^{\mu\nu}$ and the field variation $\phi \rightarrow \phi + \delta\phi$

$$\delta S = -\frac{1}{2} \int d^4x \sqrt{-g} \left[\partial_\mu\phi\partial_\nu\phi - g_{\mu\nu} \left(\frac{1}{2}g^{\alpha\beta}\partial_\alpha\phi\partial_\beta\phi + V(\phi) \right) \right] \delta g^{\mu\nu}, \quad (2.42)$$

where has been used $\delta\sqrt{-g} = -\frac{1}{2}\sqrt{-g}(g_{\mu\nu}\delta g^{\mu\nu})$. The principle of least action $\delta S = 0$ leads to the Klein-Gordon equation

$$\frac{1}{\sqrt{-g}}\partial_\mu(\sqrt{-g}g^{\mu\nu}\partial_\nu\phi) = \frac{\partial V}{\partial\phi}, \quad (2.43)$$

that can be written in a simple way

$$\ddot{\phi} + 3H\dot{\phi} = -\frac{\partial V}{\partial\phi}. \quad (2.44)$$

Where the factor $3H\dot{\phi}$ is the Hubble friction that plays a crucial role in the inflationary dynamics. With the assumption that ϕ is spatially homogeneous, $T^{\mu\nu}$ takes the form of a perfect fluid, and the energy density and pressure are given by

$$\rho = \frac{\dot{\phi}^2}{2} + V(\phi), \quad (2.45a)$$

$$P = \frac{\dot{\phi}^2}{2} - V(\phi). \quad (2.45b)$$

The dynamics during inflation are then determined from eq.(2.44) and the FRW equations eq.(2.15) by

$$H^2 = \frac{8\pi}{3m_{\text{pl}}^2} \left[\frac{\dot{\phi}^2}{2} + V(\phi) \right], \quad (2.46a)$$

$$\ddot{\phi} + 3H\dot{\phi} = -\frac{dV}{d\phi}. \quad (2.46b)$$

Where m_{pl} is the 4-th dimensional Planck mass (it is relates with the reduce Planck mass as in appendix).

2.4.5 Slow-roll approximation

The eqs.(2.46) are coupled, and we can combine them into an expression for quantified the evolution of the Hubble parameter in function to field

$$\dot{H} = -\frac{4\pi\dot{\phi}^2}{m_{\text{pl}}^2}. \quad (2.47)$$

Dividing the first equation in eq.(2.46) with eq.(2.47) is found the parameter ε in function to the field

$$\varepsilon = \frac{\dot{H}}{H^2} = \frac{\frac{3\dot{\phi}^2}{2}}{\frac{\dot{\phi}^2}{2} + V(\phi)}. \quad (2.48)$$

The condition of inflation is satisfied if $\varepsilon \ll 1$, which occurs if the kinetic contribution $\dot{\phi}^2/2$ makes a small contribution to the total energy density, this is called the slow-roll inflation [54].

In the same way it is useful to define the dimensionless acceleration per Hubble time

$$\delta \equiv -\frac{\ddot{\phi}}{H\dot{\phi}}. \quad (2.49)$$

As long as δ is small, the inflation kinetic energy stays subdominant and the inflationary expansion continues. The second slow-roll parameter defined κ , in function to field is obtained by

$$\kappa = 2(\varepsilon - \delta). \quad (2.50)$$

The condition $\varepsilon \ll 1$ implies $\dot{\phi}^2 \ll V$, which leads to the following simplification of the Friedmann equation

$$H^2 \approx \frac{8\pi V}{3m_{pl}^2}. \quad (2.51)$$

Eq.(2.51) implies, that in the slow-roll approximation, the Hubble expansion rate is determined fully by the potential and field, therefore we can rewrite the parameter ε in function of potential and field through eq.(2.47) and eq.(2.51)

$$\varepsilon \approx \frac{m_{pl}^2}{16\pi} \left[\frac{1}{V} \frac{dV}{d\phi} \right]^2. \quad (2.52)$$

To evaluate parameter δ defined in eq.(2.49), in the slow-roll approximation

$$\delta + \varepsilon = -\frac{\ddot{\phi}}{H\dot{\phi}} - \frac{\dot{H}}{H^2} \approx \frac{m_{pl}^2}{8\pi} \frac{1}{V} \frac{d^2V}{d\phi^2}. \quad (2.53)$$

A convenient way to re-defined the two potential slow-roll parameter from eq.(2.52) and eq.(2.53) is

$$\varepsilon_V = \frac{m_{pl}^2}{16\pi} \left[\frac{1}{V} \frac{dV}{d\phi} \right]^2, \quad (2.54a)$$

$$\eta_V = \frac{m_{pl}^2}{8\pi} \frac{1}{V} \frac{d^2V}{d\phi^2}. \quad (2.54b)$$

The number of e-folds realized from an initial field value can be determined analytically by [54]

$$\frac{d\phi}{dN} = \frac{m_{pl}^2}{8\pi} \left[\frac{1}{V} \frac{dV}{d\phi} \right], \quad (2.55a)$$

$$N_{\text{tot}} = \frac{\sqrt{4\pi}}{m_{pl}} \int_{\phi_{\text{end}}}^{\phi_0} \frac{d\phi}{\sqrt{\varepsilon_V}}. \quad (2.55b)$$

Where ϕ_0 and ϕ_{end} are the field values at the boundaries of the interval where is valid $\varepsilon_V < 1$.

2.4.6 Initial conditions

In this section we will suppose a spatially varying fluctuation on inflation. The coupling to the metric will lead to mixing between the inflation fluctuations $\delta\phi$ and the metric fluctuations $\delta g_{\mu\nu}$. The line element defined in eq.(2.1), for the scalar fluctuations takes the form

$$ds^2 = a^2(\eta) \left[-(1 + 2A)d\eta^2 + 2\partial_i B dx^i d\eta + \delta_{ij} dx^i dx^j \right]. \quad (2.56)$$

Where the metric fluctuations A and B are related to the inflation fluctuations $\delta\phi$ through the Einstein equations. Varying of the action defined in eq.(2.41) with $\phi(x, t) = \bar{\phi}(t) + \delta\phi(x, t)$ and $\sqrt{-g} = a^4(1 + A)$, we get the motion equation [1]

$$\delta\phi'' + 2\mathcal{H}\delta\phi' - \nabla^2\delta\phi = (A' + \nabla^2 B)\bar{\phi}' - 2a^2V_{,\phi}A - a^2V_{,\phi\phi}\delta\phi, \quad (2.57)$$

where $\mathcal{H} = aH$, $\phi' = d\phi/dx$, $\phi'' = d^2\phi/dx^2$, $V_{,\phi} \equiv dV/d\phi$ and $V_{,\phi\phi} \equiv d^2V/d\phi^2$. The Einstein equations can be used to eliminate the metric perturbations A and B in eq.(2.57)

$$A = \varepsilon \frac{\mathcal{H}}{\bar{\phi}'} \delta\phi, \quad (2.58a)$$

$$\nabla^2 B = -\varepsilon \frac{\mathcal{H}}{\bar{\phi}'} (\delta\phi' + (\delta - \varepsilon)\mathcal{H}\delta\phi), \quad (2.58b)$$

where the slow-roll parameters defined in eq.(2.54) are written in terms of $\bar{\phi}$ as $\varepsilon \rightarrow \varepsilon(\bar{\phi})$ and $\delta \rightarrow \delta(\bar{\phi})$. The eq.(2.57) can be rewritten in a simpler form

$$\delta\phi'' + 2\mathcal{H}\delta\phi' - \nabla^2\delta\phi = \left[(3 + 2\varepsilon - \delta)(\varepsilon - \delta) - \frac{\delta'}{\mathcal{H}} \right] \mathcal{H}^2 \delta\phi. \quad (2.59)$$

The eq.(2.59) can be written in a compact shape if we define $f \equiv a\delta\phi$, then we get the so-called Mukhanov-Sasaki equation [1; 54]

$$f'' + \left(k^2 - \frac{z''}{z} \right) f = 0. \quad (2.60)$$

Where $z \equiv a\bar{\phi}'/\mathcal{H} = a\sqrt{2\varepsilon} \text{ Mpl}$.

2.4.7 Power spectrum of primordial curvature perturbations

We saw in the previous section, that the primordial fluctuations are quantified through the field $f(\eta, x)$ in eq.(2.60). These primordial fluctuation can be defined as quantum fluctuation with the respective operator $\hat{f}(\eta, x)$. In the vacuum state we have

$$\langle |\hat{f}| \rangle = 0, \quad (2.61a)$$

$$\langle |\hat{f}|^2 \rangle = \int \frac{d^3k}{(2\pi)^3} |f_k(\eta)|^2. \quad (2.61b)$$

Where $f_k(\eta)$ is the Fourier mode function and depend only on the magnitude of the comoving Fourier wavenumber k . The variance of the quantum fluctuations is determined by the power spectrum [1]

$$P_{\mathcal{R}}(k) \equiv \frac{k^3}{2\pi^2} |f_k(\eta)|^2. \quad (2.62)$$

The parameter $P_{\mathcal{R}}(k)$ in eq.(2.62), is so-called as the primordial curvature perturbations, and is the bridge between inflation and the late Universe. The observed scalar power spectrum of the CMB is in general, described by the power law of the momentum k [56]

$$P_{\mathcal{R}}(k) = \mathcal{A}_s \left(\frac{k}{k_\star} \right)^{n_s - 1 + \frac{1}{2} \alpha_s(k) \ln(k/k_\star)}. \quad (2.63)$$

Where the amplitude \mathcal{A}_s and the spectral index or tilt n_s are observable parameters, k_\star is the pivot scale of the experiment, and the tilt running α_s is a function that depends on the inflationary model. One of the goals of current precision cosmology is to measure these quantities by, e.g., observing the polarization of the CMB [57; 58; 59]. The ever-tighter constraints [40; 60; 61; 62; 63; 64; 65] on these observables and the ratio r of the tensor and scalar amplitudes (associated with the gravitational wave background [66; 67; 68]) offer an opportunity to discriminate among the various existing inflationary models (see e.g. [69] for a large

classification). The scalar spectral index is defined as

$$n_s - 1 \equiv \frac{d \ln P_{\mathcal{R}}(k)}{d \ln k}, \quad (2.64)$$

using $k = aH$ in eq.(2.64), and using the slow-roll parameters evaluated in the pivot scale k_*

$$n_s = 1 - 2\varepsilon_* - \kappa_*. \quad (2.65)$$

The power spectrum amplitude is defined as [40]

$$\mathcal{A}_s = \frac{V}{24\pi^2 \varepsilon_V} \Big|_{\phi=\phi_*}. \quad (2.66)$$

which for the best Planck fit's value is $\ln(10^{10} \mathcal{A}_s) = 3.0448$ and $n_s = 0.9649 \pm 0.0042$ [70].

Chapter 3

Thermalization and Spectral distortions

In the early Universe, photons and baryons are tightly coupled, behaving as a single viscous fluid close to thermal equilibrium due to Compton scattering (CS), Bremsstrahlung (BR), and double Compton scattering (DC), processes that isotropize the photon-baryon fluid. However, early energy injection into the photon-baryon fluid can disrupt thermal equilibrium, causing the CMB to experience small departures from the blackbody distribution. These deviations are known as spectral distortions and are sensitive to any energy injected into the CMB at different epochs. The CMB SD complements the anisotropy CMB observations and provide a new benchmark to test standard and non-standard cosmological scenarios.

3.1 The Boltzmann equation

The Boltzmann equation gives us information for the rate of change in time of a given particle through its distribution function f

$$\frac{df}{dt} = C[f]. \quad (3.1)$$

The right-hand side in eq.(3.1) contains all possible collision terms; in the absence of collisions, we have $df/dt = 0$ [39]. Suppose that the distribution function depends on time t , position x , and the moment p . Here x and p are the 4-position and 4-momentum for photons,

respectively, we can write the left-hand side of eq.(3.1) as

$$\frac{df}{dt} = \frac{\partial f}{\partial x^\mu} \frac{dx^\mu}{dt} + \frac{\partial f}{\partial p^\mu} \frac{dp^\mu}{dt}, \quad (3.2)$$

taking account the direction vector, $\hat{p}^i = \hat{p}_i$, which by definition satisfies $\delta_{ij}\hat{p}^i\hat{p}^j = 1$, we can write eq.(3.2) as

$$\frac{df}{dt} = \frac{\partial f}{\partial t} + \frac{\partial f}{\partial x^i} \cdot \frac{dx^i}{dt} + \frac{\partial f}{\partial p} \frac{dp}{dt} + \frac{\partial f}{\partial \hat{p}^i} \cdot \frac{d\hat{p}^i}{dt}. \quad (3.3)$$

If we considered the photons in the perturbed FRW Universe, with Φ and Ψ as the perturbation in the metric and the spatial curvature respectively, we have [39]

$$\frac{dx^i}{dt} = \frac{\hat{p}^i}{a} (1 + \Phi - \Psi), \quad (3.4a)$$

$$\frac{1}{p} \frac{dp}{dt} = -H - \frac{\partial \Phi}{\partial t} - \frac{\hat{p}^i}{a} \frac{\partial \Psi}{\partial x^i}. \quad (3.4b)$$

Introducing eqs.(3.4) in eq.(3.2), and collecting terms we can rewritten eq.(3.2)

$$\frac{df}{dt} = \frac{\partial f}{\partial t} + \frac{\hat{p}^i}{a} \frac{\partial f}{\partial x^i} - p \frac{\partial f}{\partial p} \left[H + \frac{\partial \Phi}{\partial t} + \frac{\hat{p}^i}{a} \frac{\partial \Psi}{\partial x^i} \right]. \quad (3.5)$$

The right-hand side of eq.(3.1) is more difficult to describe because it depends on all species and the respective interaction between them. For example, if we consider CS, the scattering process of interest is

$$e^-(\mathbf{q}) + \gamma(\mathbf{p}) \longleftrightarrow e^-(\mathbf{q}') + \gamma(\mathbf{p}'), \quad (3.6)$$

the collision coefficient will be described as the sum over all momentum $(\mathbf{q}, \mathbf{q}', \mathbf{p}')$ which affect the photon distribution $f(\mathbf{p})$

$$C|f(\mathbf{p})| = \sum_{\mathbf{q}, \mathbf{q}', \mathbf{p}'} |\text{Amplitude}|^2 \{f_e(\mathbf{q}')f(\mathbf{p}') - f_e(\mathbf{q})f(\mathbf{p})\}. \quad (3.7)$$

Where the parameter $|\text{Amplitude}|^2$ is the Lorentz invariant matrix element, f is the photon distribution and f_e is the electron distribution function [71]. In the next section, we will write the Boltzmann equation eq.(3.1) for photons with the explicit collision coefficient for CS, BR

and DC.

3.2 Thermalization of CMB spectral distortions

The CMB exhibits a perfect blackbody frequency spectrum, given by the precision of the measurements. At high redshifts $z \gtrsim 10^8 - 10^9$, the thermalization of CMB spectral distortions is extremely efficient. Therefore, the study of CMB SD is restricted at redshift below $z \lesssim 10^8$. During the subsequent evolution of the Universe, the main interactions between the photons and matter are governed by CS, DC scattering, and BR as we mentioned in the previous section, these interactions became inefficient below $z \lesssim 10^7$ [16; 72; 73]. The thermalization problem can be formulated by solving the Boltzmann equation in the expanding Universe and the interaction evolution with free electrons (and baryons) [71].

3.2.1 Evolution of the photons in the Universe

We wrote the Boltzmann equation for photons in the previous section, here we will write the evolution of the photon phase space distribution more simply as $f = n_\gamma(x^\mu, p^\mu)$. In this section, we consider the Boltzmann equation in an isotropic and homogeneous FRW Universe, which implies $\partial\Phi/\partial t = 0$, $\partial\Psi/\partial t = 0$, and $\partial n_\gamma/\partial x^i = 0$. From eq.(3.5) we have

$$\frac{\partial n_\gamma}{\partial t} - Hp \frac{\partial n_\gamma}{\partial p} = C[n_\gamma]. \quad (3.8)$$

Where $n_\gamma(x^\mu, p^\mu) \rightarrow n_\gamma(t, p)$. The collision term in the Boltzmann equation have several important effects. Most importantly, CS couples photons and electrons, keeping the two in close thermal contact until low redshifts $z \simeq 100 - 200$. BR and DC allow adjusting the photon number and are especially fast at low frequencies [74]. The descriptions of collision terms for CS, DC, and BR determine the extent to which the CMB can be thermalized. The right-hand side of eq.(3.8) can be written as a sum of terms describing the different interactions of the particles

$$C[n_\gamma] = \left. \frac{dn_\gamma}{d\tau} \right|_{\text{CS}} + \left. \frac{dn_\gamma}{d\tau} \right|_{\text{DC+BR}}. \quad (3.9)$$

In eq.(3.9) has been introduced the optical depth $d\tau = N_e\sigma_T dt$ with N_e the electron numerical density and σ_T the Thomson cross-section.

Collision term for Compton scattering

The dominant interaction that thermally couples photons and electrons before recombination is the CS, this interaction is responsible for redistributing photons in energy. The CS term in eq.(3.9) accounts for the comptonization of photons by free thermal electrons, we can use the so-call Kompaneets equation [74]

$$\left. \frac{dn_\gamma}{d\tau} \right|_{\text{CS}} \approx \frac{\theta_e}{x^2} \frac{\partial}{\partial x} x^4 \left[\frac{\partial n_\gamma}{\partial x} + \frac{T_\gamma}{T_e} n_\gamma (n_\gamma + 1) \right]. \quad (3.10)$$

Where $T_\gamma = T_0(1+z)$ is the photon temperature, $\theta_e = k_B T_e / m_e$ is the dimensionless electron temperature with m_e as the electron mass, T_e is the electron temperature, $x = h\nu / k_B T_\gamma$ is the photon frequency dimensionless, and k_B is the Boltzmann constant. The eq.(3.10) is obtained by computing the Compton collision term in eq.(3.7), at the limit of $h\nu \ll kT_e$ and $hT_e \ll m_e$. The first term into the brackets is associated to small shift in the observed frequency induced by electrons with relativistic velocities, this known as Doppler broadening and Doppler boosting, and the second term accounts for the recoil effect and stimulated recoil [75]. These latter terms are especially important for reaching full equilibrium in the limit of many scatterings [74].

Collision term for Double Compton scattering and Bremsstrahlung

In the early Universe the responsible of photon production and absorption are BR



where X is an ion, and the DC scattering



The term associated with the contribution of double Compton scattering and Bremsstrahlung in eq.(3.9) can be written as [76]

$$\left. \frac{dn_\gamma}{d\tau} \right|_{\text{DC+BR}} = \frac{K_{\text{BR}} e^{-x_e} + K_{\text{DC}} e^{-2x}}{x^3} [1 - n_\gamma(e^{x_e} - 1)]. \quad (3.13)$$

Where $x_e = hv/k_B T_e$ is the electron dimensionless frequency, K_{BR} and K_{DC} are the emission coefficient contribution from Bremsstrahlung and double Compton scattering, respectively. In the thermally coupled photons with electrons we can approximate $T_e \approx T_\gamma$ at $z \gtrsim 10^3$, we have

$$K_{\text{BR}} \simeq 1.4 \times 10^{-6} \left[\frac{\bar{g}_{\text{ff}}}{3.0} \right] \left[\frac{\Omega_b h^2}{0.022} \right] (1+z)^{-1/2}, \quad (3.14a)$$

$$K_{\text{DC}} \simeq 1.7 \times 10^{-20} (1+z)^2. \quad (3.14b)$$

Where \bar{g}_{ff} is the BR gaunt factor. Coefficient in eqs.(3.14) implies that $z_{\text{dc,br}} \simeq 3.7 \times 10^5 \left(\left[\frac{\bar{g}_{\text{ff}}}{3.0} \right] \left[\frac{\Omega_b h^2}{0.022} \right] \right)^{2/5}$ BR and DC emissions are similarly important. At $z > z_{\text{dc,br}}$, DC emission is more crucial, while at lower redshifts BR dominates [71; 76].

Electron-temperature term

The right term in the left-hand side in eq.(3.1) arises because the electron and photon evolve with time [77]

$$H p \frac{\partial n_\gamma}{\partial p} = x \frac{\partial n_\gamma}{\partial x} \frac{\partial}{\partial t} \left[\ln \left(\frac{T_e}{T_0(1+z)} \right) \right], \quad (3.15)$$

the electron temperature is given by

$$\frac{dT_e}{dt} = -2HT_e - \frac{4\sigma_T \rho_\gamma}{3m_e f_\star} \left(T_e - \frac{1}{\rho_\gamma \pi^2} \int_0^\infty p^4 n_\gamma (1+n_\gamma) dp \right). \quad (3.16)$$

Where f_\star includes the correction due to baryons $f_\star = [(1+X_e)/2 - (3+2X_e)Y_p/8] (1 - Y_p/2)^{-1} x_e$ with the ionization fraction of electrons X_e and the primordial helium mass fraction $Y_p = 0.25$. In the right-hand side of eq.(3.16) the first term is associated to Compton cooling, and the second term dominates in the high tightly coupled between photon-electrons, in this case is obtained $T_e(z) \simeq T_0(1+z)$ [77].

3.3 Analytic descriptions for μ and y distortion

In the previous section, we have given a formulation of the thermalization problem, including all the relevant collision terms in eq.(3.1). In this section, we want to present an analytic approximation for CMB μ and y -SD. As it has been said before, CMB SD depends on the energy injection time, at very early times ($z \lesssim 10^8$), no spectral distortion could be created, since it would simply result in a shift of the blackbody temperature ΔT . Below to $z \sim 2 \times 10^6$ the CMB spectrum is sensitive to an effective chemical potential μ since processes as double Compton scattering become inefficient ($3 \times 10^5 \lesssim z \lesssim 2 \times 10^6$). At a later time, the CMB is mostly sensitive to the y -distortion ($z \lesssim 10^4$), which quantifies the amount of energy transfer via Compton scattering, which becomes less efficient [16; 25]. These arguments have been used for formulating an analytic theory for μ and y -SD.

For small spectral distortions ($\mu, y \ll 1$) can be written an analytical set of equations for the description of μ and y -distortion. Some considerations are made in eq.(3.1): it is assumed that photons and electrons are in thermal equilibrium, therefore, their temperature is the same $T_\gamma = T_e$ and is used $T_\gamma = T_z = T_0(1+z)$ for high redshift. It is assumed that when radiation dominates the evolution of the Universe, the CS is extremely efficient, and photons evolve along a sequence of equilibrium spectra [71; 76]. Therefore, is assumed that one or more of the three processes are effective enough to establish quasi-static conditions. The last assumption allows us writes the solution of the photon distribution n_γ as

$$n_\gamma \simeq n_{\text{pl}} + \Delta n_\gamma \approx n_{\text{pl}} + \Delta n_\gamma^\mu + \Delta n_\gamma^y, \quad (3.17)$$

where the full SD CMB is given by $\Delta n_\gamma \equiv \Delta n_\gamma^\mu + \Delta n_\gamma^y$, this can be written in the intensity units as

$$\Delta I = 2h\nu^3 \Delta n_\gamma. \quad (3.18)$$

Where n_{pl} is the Planck distribution function associated with the perfect blackbody, produced in the thermalization process of photon and Δn_γ corresponds just to a departure of the blackbody shape and is associated with all photon interaction [74].

3.3.1 The μ -spectral distortion

In the early Universe, many scatterings are taking place and the redistribution of photons in frequency is very efficient, this regimen is found at $3 \times 10^5 \lesssim z \lesssim 2 \times 10^6$ and the distortion is given by a chemical potential μ -distortion. As we mentioned before, we assume that Boltzmann equation defined in eq.(3.1), can be approximated by neglecting emission and absorption processes, and eq.(3.9) becomes quasi-stationary [71; 74]

$$0 \approx \left. \frac{dn_\gamma}{d\tau} \right|_{CS}, \quad (3.19)$$

where the right-hand side is the term described with eq.(3.10). The solution of eq.(3.19) is given by

$$\Delta n_\gamma^\mu \equiv \left. \frac{\delta n_\gamma}{n_\gamma} \right|_\mu = \mu \left[\frac{xe^x}{e^x - 1} \left(0.4561 - \frac{1}{x} \right) \right]. \quad (3.20)$$

Where μ is the chemical potential in the Bose-Einstein function distribution, and is obtained with the statistical relations defined in eqs.(2.30) and supposing a full energy injection $\mu = \int \dot{Q} dt$

$$\mu \simeq 1.4 \int_0^\infty dz \frac{d(Q/\rho_\gamma)}{dz} \mathcal{J}_\mu(z). \quad (3.21)$$

Where $\mathcal{J}_\mu(z)$ defines the spectral μ -distortion visibility function and parametrizes the thermalization efficiency for μ -distortion, the shape of this function is shown in the appendix A.1. The factor $d(Q/\rho_\gamma)/dz$ quantifies the energy release caused by some external physical process at redshifts range $3 \times 10^5 \lesssim z \lesssim 2 \times 10^6$.

3.3.2 The y -spectral distortion

At redshifts $z \lesssim 5 \times 10^4$ the redistribution of photons in frequency becomes inefficient, and the distortion is given by the y -distortion. If the electrons are strongly heated, $T_e/m_e \gg p/m_e$, we can assume that in the Boltzmann equation eq.(3.1), can be neglected the photon emission [71], and we can write

$$\frac{dn_\gamma}{d\tau} \approx \left. \frac{dn_\gamma}{d\tau} \right|_{CS}, \quad (3.22)$$

once again, the right-hand side is the term described in eq.(3.10). The solution of eq.(3.22) is given by

$$\Delta n_\gamma^y \equiv \frac{\delta n_\gamma}{n_\gamma} \Big|_y = y \left[\frac{x e^x}{e^x - 1} \left[x \left(\frac{e^x + 1}{e^x - 1} \right) - 4 \right] \right]. \quad (3.23)$$

Where y is the so-called Compton- y distortion, this was first studied for the hot electrons residing inside in the potential wells of clusters of galaxies, giving rise to the thermal Sunyaev-Zeldovich (SZ) effect [74]. The y -distortion can be obtained with the statistical relations defined in eqs.(2.30) and supposing a full energy injection $y = \int \dot{Q} dt$

$$y \simeq \frac{1}{4} \int_0^\infty dz \frac{d(Q/\rho_\gamma)}{dz} \mathcal{J}_y(z). \quad (3.24)$$

Where $\mathcal{J}_y(z)$, similar as in the previous section, defines the spectral y -distortion visibility function and parametrizes the thermalization efficiency for y -distortion, the shape of these function is showed in the appendix A.1. The factor $d(Q/\rho_\gamma)/dz$ quantifies the energy release caused by some external physical process at redshifts $z \lesssim 10^4$.

In the next chapters, we describe in details the term $d(Q/\rho_\gamma)/dz$ for two different cases, and show the main results of this thesis for decaying dark particles and damping of primordial small-scale perturbations. The amplitudes of the SD (eq.(3.21) and eq.(3.24)) are directly linked to the total energy that was released over the cosmic history.

Chapter 4

Spectral distortions from dark sector

4.1 QCD dark matter scenario

The dark-sector hadronization may have a collection of dark bound states that, depending on the complexity of the undergoing model, is likely to have dark particles with different mass, lifetime, charge, etc. For instance, at the QCD confinement scale, Λ_{QCD} , gauge invariant states are created forming color-neutral particles, mesons (e.g. pions π), and baryons (e.g. protons and neutrons), with non-perturbative masses generated and being proportional to Λ_{QCD} (e.g. $m_\pi \simeq 140 \text{ MeV}$, $m_n \simeq 940 \text{ MeV}$) much larger than the quark masses ($m_u \simeq 2.3 \text{ MeV}$, $m_d \simeq 4.8 \text{ MeV}$). From a dimensional analysis of spontaneous symmetry breaking theories, the mass of the dark bound states is due to the underlying gauge force and proportional to the confinement energy scale, i.e. $m_\chi \propto \Lambda_c$. Examples of this, beyond QCD, are the gauge-mediated SUSY breaking model [78]. With no constraints on the dark sector theory, masses of the bound states can also be much larger than the energy transition, $m_\chi \ll \Lambda_c$.

In QCD, mesons are particles that have a short life span compared to baryons: e.g., the proton has a long lifetime, since no decay has been detected its lifetime is $\mathcal{O}(10^{32})$ yr, neutron decays into protons with a lifetime of $\mathcal{O}(10^3)$ s, and charged pions have a lifetime of $\mathcal{O}(10^{-9})$ s. Some dark particles may be electrical neutral and stable particles (i.e. dark baryons) that could be good candidates for CDM or WDM, depending on the velocity dispersion v_c at the confinement epoch it could describe one candidate or another. On the other hand, unstable

(short-lived) dark particles can also be expected, i.e. dark mesons, that decay after the confinement scale and deposit a fraction of their energy, into the SM photons through a coupling of the SM and the dark sector. The energy deposited to the photons could produce SD, we aim to compute the relation between the confinement phenomenological parameters and the magnitude of the SD.

We assume a model whose dynamics give rise to a phase transition at an energy scale Λ_c based on gauge theory and has a structure similar to the standard QCD model. In this gauge dark group that is by hypothesis not contained in the standard model of particles, its dynamic at energies larger than $\Lambda_c(a_c)$ the dark elementary fields are nearly massless and are relativistic, they behave as radiation. Below the cosmological scale a_c a phase transition takes place due to a strong gauge coupling constant, and dark elementary fields bind together producing bound states, that is, particles acquire a non-perturbative mass. Since the bound states are more massive than the elementary particles, the resulting velocity dispersion of the i -particle after the transition, $v_{c,i}$ is significantly reduced compared to the elementary fields. The particles are relativistic and with a very small mass before the transition, $a < a_c$, they behave as relativistic particles. In contrast, after the transition, $a > a_c$, the particles acquired a non-perturbative mass with an initial velocity dispersion v_c , depending on the value of v_c , the particle may still be in a relativistic regime, which is an interesting case but hard to distinguish from thermal WDM particle, the velocity $v_c \leq 1/\sqrt{2}$, define the non-relativistic regime which is when the momentum of the particle equals its inertial mass. Therefore, the equation of state that describes this behavior is given by [45]

$$\omega_{dm} = \begin{cases} \frac{1}{3} & \text{for } a < a_c \\ \frac{1}{3}v^2 & \text{for } a > a_c \end{cases}, \quad (4.1)$$

where the velocity of particles is given by

$$v(a) = \frac{\gamma_c v_c (a_c/a)}{\sqrt{1 + \gamma_c^2 v_c^2 (a_c/a)^2}}, \quad (4.2)$$

where we have used $\gamma_c \equiv (1 - v_c^2)^{-1/2}$. The pressure is given by the equation of state $P = \omega\rho$.

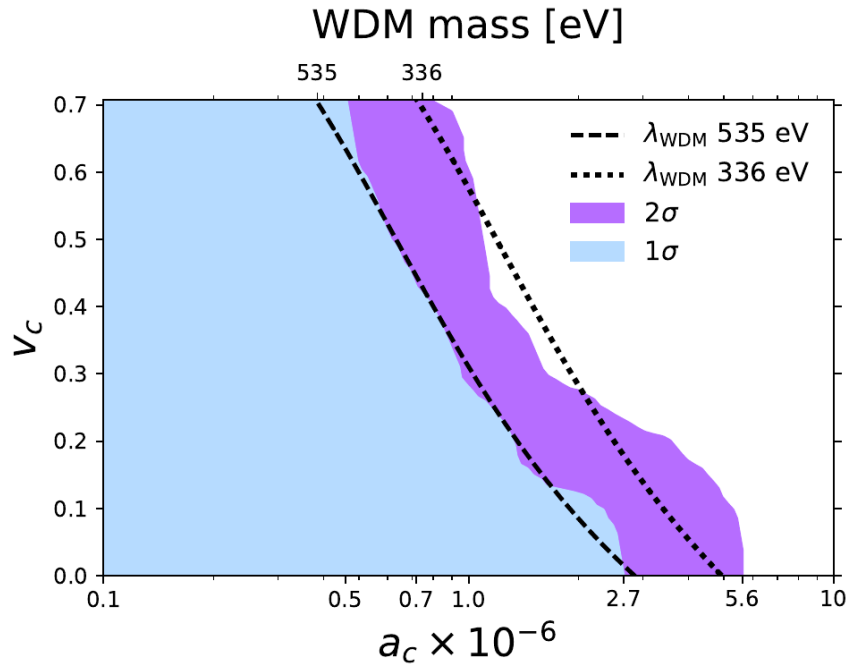


Figure 4.1: Likelihoods for parameters on the BDM model, a_c and v_c , from MonteCarlo simulations using MontePython with Planck 2018, type Ia SN, and BAO data. Light blue region represent 2σ likelihood, where largest values of a_c are still valid. Purple region is the 1σ likelihood. Figure taken from [45].

Therefore, the dark matter energy density in the QCD dark matter scenario is

$$\rho_{\text{dm}}(a) = \rho_{\text{dm}0} \left(\frac{a}{a_0} \right)^{-4} \left(\frac{v_0}{v(a)} \right), \quad (4.3)$$

where v_0 is obtained with eq.(4.2) evaluated today, $v(a_0) = v_0$. When $a_c \ll a_0$ and $a_0 \ll a$ we have

$$\frac{v_0}{v(a)} \sim \frac{a}{a_0}, \quad (4.4)$$

since the last quantity is a constant, the fluid behaves as matter.

In the work [45] are presented constraints for the Bound Dark Matter (BDM) model, with CMB Planck, supernova SNIa, and baryon acoustics oscillation data were used to established a valid region at 1σ and 2σ in the parameter space $a_c - v_c$ (see figure 4.1). In an extreme case, the upper bound was put at $a_c < 2.66 \times 10^{-6}$ for $v_c = 0$ at 1σ (for CDM particles). Also was evaluated the case of $a_c = 3.18 \times 10^{-8}$ for $v_c = 1/\sqrt{2}$, (for WDM articles). In this sense,

we are interested in a set of $a_c - v_c$ parameters constraints at 1σ and 2σ for simulations that will be presented in the next section of our framework. We assume that at least one kind of long-life and short-life particles are created, and that the minimum number of particles that the short-life particles could decay into is two.

On the one hand, we have particles with a long life-time, neutral dark-flavor, non-perturbative mass, and an initial velocity dispersion v_c after the transition. Depending on the value of v_c this particle may describe the features of CDM, i.e. $v_c \sim 0$, or it could also describe WDM if it has a non-negligible velocity v_c that contributing to the free-streaming even after the transition. The minimum number of fundamental dark fields needed to form a bound state is two, with the opposite dark-flavor sign, χ_q and $\chi_{\bar{q}}$. The constituent dark model would give us the dynamics of the bound $\chi_q\chi_{\bar{q}}$ states grouped into SU(N) dark-flavor multiplets. Multi- χ_q singlet states may also exist, but the larger number of χ_q particles implied a lower probability of being created, then it is assumed that a partial amount of the energy of this short-life bound state of the dark group, is deposited into photons of the standard model

$$\chi_q\chi_{\bar{q}} \rightarrow \chi_{\text{short-life}} \rightarrow \gamma. \quad (4.5)$$

To compute the mass of the constituted particle, we would need to make the calculations using relativistic quantum field theory, where bound states are identified by the occurrence of poles of corresponding amplitudes or Green functions with appropriate quantum numbers. These poles have a nonperturbative character, whose properties depend on the integral equations among amplitudes and Green functions, using the specific structure of a Lagrangian for the dark particles, which is out of the scope of this work. However, for a first-order correction, the computation for the mass of the bound state is given by

$$m_\chi \simeq 2m_q + \Lambda_c. \quad (4.6)$$

The last expression is obtained assuming that the coupling constant is weak, but from dimensional analysis, this is still valid for a strong coupling constant. For instance, in QCD the mass of the bound state is dominated by the binding energy, like the pion whose mass is

$m_\pi \simeq 140\text{MeV}$, or the neutron mass $m_n \simeq 940\text{MeV}$, in both cases, the mass is much larger than the quark masses ($m_u \simeq 2.3\text{MeV}$, $m_d \simeq 4.8\text{MeV}$). If m_q is small compared to Λ_c , the eq.(4.6) can be approximated as $m_\chi \simeq \Lambda_c (1 + 2m_q/\Lambda_c) \equiv \alpha\Lambda_c(a_c)$. From energy and momentum conservation equations for the decay process, the equation of the energy of photons produced is

$$E_\gamma = \Sigma_\chi \frac{\alpha\Lambda_c}{2}. \quad (4.7)$$

Where Σ_χ is the fraction of the bound states of the dark group transferring any energy to the CMB photons, and the factor $1/2$ is for the case of two photons as the most probable interaction.

4.2 Decaying dark particle scenario

The key feature in the model worked here is an abrupt transition of the dark matter equation of state, as we mentioned in the previous section. This is a consequence of the phase transition at energy scale Λ_c at scale factor a_c . We assume that two kinds of dark particles are formed after a_c , a long-life stable, and a short-life unstable particle. Therefore, we need to define the net volumetric rate of heat injection $d(Q/\rho_\gamma)/dz$ in the process for decaying particles in a time τ_χ . For $a < a_c$ there is no energy transfer to photons, this means $d(Q/\rho_\gamma)/dz = 0$. In a comoving frame, the number of particles N obeys the exponential decay, for the unstable particle before phase transition in an expansion Universe $N_\chi(z) = N_{\text{dm}}(z)e^{-\Gamma_\chi(t(z)-t_c)}$, where t_c is the time when the unstable particle is created, we can write the energy density as $\rho_\chi(z) = \Sigma_\chi \rho_{\text{dm}}(z)e^{-\Gamma_\chi(t-t_c)}$, where $\rho_\chi(z)$ is the energy density evolution of the decaying particle and ρ_{dm} is the energy density of the dark matter defined in eq.(4.3). The rate of transfer energy, \dot{Q} is given by $\dot{Q} = d\rho/dt$, is usually assumed in this scenario to have a short lifetime [34]. However, there are no constraints on the lifetime of particles in the dark sector, and we certainly do not make any assumptions about the lifetime and the energy injection rate will depend on the time evolution of the individual particle energy E and the number density, N as this last parameter carries the decay behavior. We can write the energy rate as,

$$\dot{Q} = \dot{\rho}_\chi(z)e^{-\Gamma_\chi(t-t_c)} - \rho_\chi(z)\Gamma_\chi e^{-\Gamma_\chi(t-t_c)}, \quad (4.8)$$

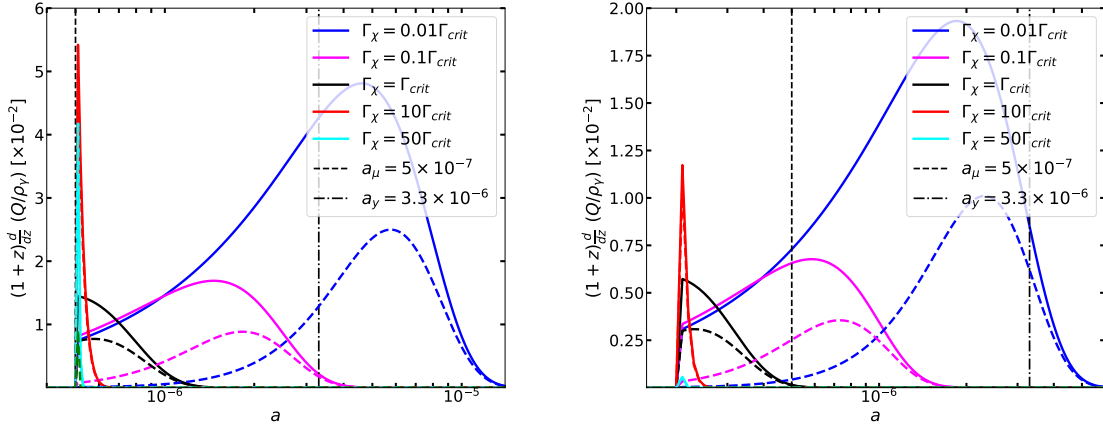


Figure 4.2: Function dQ/dz calculated for $v_c = 0.01$ in $a_c = 5 \times 10^{-7}$ (left) and $a_c = 1.99 \times 10^{-7}$ (right), with $\Gamma_{crit} = 5.90 \text{ yr}^{-1}$ and $\Gamma_{crit} = 36.82 \text{ yr}^{-1}$ respectively. Vertical dotted lines are related with μ scale factor region.

then, we use the continuity equation, $\dot{\rho}_\chi + 3H(\rho_\chi(z) + P) = 0$, to simplify the last expression and change the time derivative to redshift derivatives and, written in a dimensionless shape, we arrive at the expression

$$\frac{d(Q/\rho_\gamma)}{dz} = \frac{\Gamma_\chi \Sigma_\chi \rho_{dm} e^{-\Gamma_\chi(t-t_c)}}{\rho_\gamma H(1+z)} \left[1 + \frac{\Gamma_{crit}}{\Gamma_\chi} \right]. \quad (4.9)$$

Where $\Gamma_{crit} \equiv 3H(1 + \omega_\chi)$ is a time-dependent parameter proportional to the rate of expansion of the Universe. The eq.(4.9) gives naturally two regimes, the first $\Gamma_\chi \gg \Gamma_{crit}$ when the rate of decay of the particle is greater than the expansion of the Universe, this describes well a short lifetime particles and is reduced to previous results. The second one, when $\Gamma_\chi \ll \Gamma_{crit}$, we have long lifetime particle after the production of the decaying particles, a term that cannot be ignored and introduces a rich of new possible scenarios. Now considering the last term on eq.(4.9) could lead to an underestimation of the energy rate, as can be seen in figure 4.2.

In eq.(4.9) the energy density $\rho_{dm} = \rho_{dm}(z, a_c, v_c)$ is the dark matter energy density function, modified from the energy density introduced in chapter 2, and in this framework is a function of the scale of transition, a_c , and the initial velocity of the particle, v_c . In order to visualize the shape of eq.(4.9) we have plotted in figures 4.2 and 4.3, the heating rate evolution for some scenarios of our interest. First was plotted in figure 4.2 for $\Gamma_{crit} = 5.9 \text{ yr}^{-1}$ and

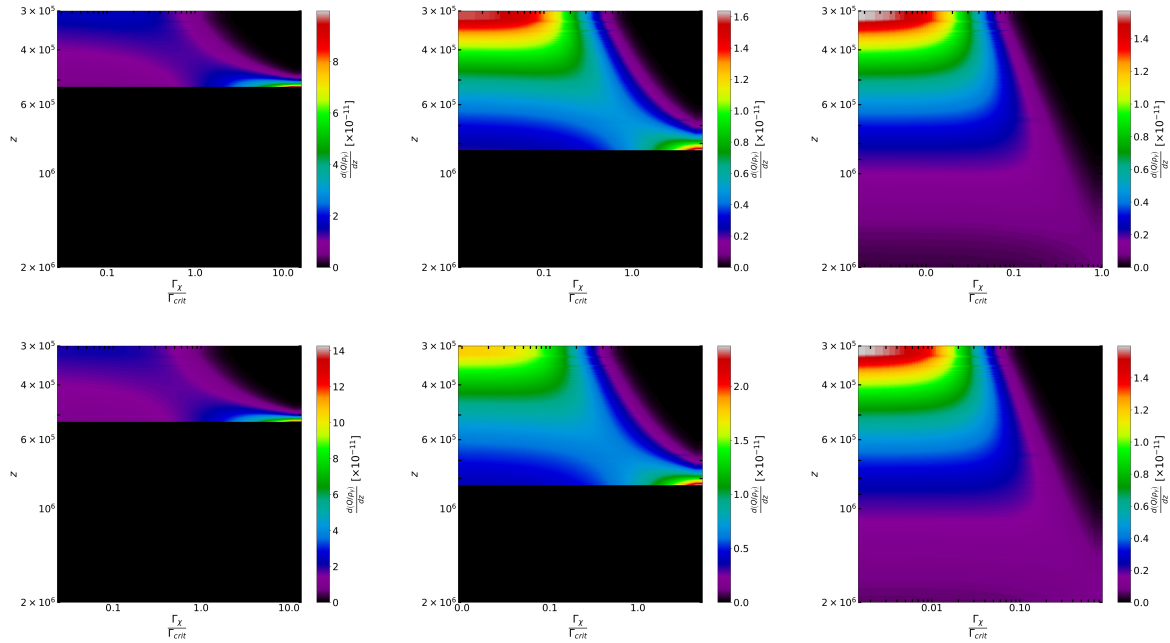


Figure 4.3: Using eq.(4.9) we show the effective heating parametrization varying $\Gamma_\chi = [0.01, 3] \text{ yr}^{-1}$, for $v_c = 0.01$ (top) and $v_c = 0.71$ (bottom) at $a_c = 2 \times 10^{-6}$ (left), 1.25×10^{-6} (middle) and 5×10^{-7} (right), this values are representative of the μ region $[3.3 \times 10^{-6}, 4.9 \times 10^{-7}]$. In this plot was used $\Gamma_{\text{crit}} = [0.37, 0.94, 5.89]$ for the respective value of a_c considered.

$a_c = 5 \times 10^{-7}$ (left), $\Gamma_{\text{crit}} = 36.8 \text{ yr}^{-1}$ and $a_c = 1.99 \times 10^{-7}$ (right) with $v_c = 0.01$, $\Sigma_\chi = 10^{-4}$ and $\Gamma_\chi = 0.001\Gamma_{\text{crit}}, 0.1\Gamma_{\text{crit}}, \Gamma_{\text{crit}}, 10\Gamma_{\text{crit}}, 50\Gamma_{\text{crit}}$. Two types of curves are shown, first with the eq.(4.9) completed (solid curve) and with $\Gamma_{\text{crit}}/\Gamma_\chi \equiv 0$ (dash-dotted curves). These curves were plotted over a large range of scale factor, and they show how the maximal of the curves arise inside or outside of μ region. Can also be seen in figure 4.2 the discrepancy between the curves, when we take account the factor $\Gamma_{\text{crit}}/\Gamma_\chi$. Secondly, in figure 4.3 the heating rate is shown for $v_c = 0.01$ (top panel) and $v_c = 0.71$ (bottom panel) with $a_c = 2 \times 10^{-6}$ (left), 1.25×10^{-6} (middle) and 5.25×10^{-6} (right) for $\Gamma_\chi = [0.01, 3] \text{ yr}^{-1}$. Notice that the redshift or the scale factor was restricted approximately at the μ regimen ($2 \times 10^6 \lesssim z \lesssim 3 \times 10^5$). In table 4.1 we show the values that we run for a_c , v_c , Γ_χ and Σ_χ , these were taken in order to use the results at 1σ and 2σ reported in work [45], they run a Monte Carlo chain with Planck, Supernova Ia and BAO data. For our purpose, we also restricted the values of a_c to the μ redshift range, and v_c was running for cold, warm, and hot dark particles. For the range of values of Σ_χ we took the range constrained at work [34], in which they showed bounds at 95% on the

parameter	values	Δ
Σ_χ	$[10^{-7}, 10^{-3}]$	9×10^{-8}
Γ_χ	$[0.01, 3] \text{ yr}^{-1}$	$3 \times 10^{-10} \text{ yr}^{-1}$
v_c	$[0.01, 0.99]$	2×10^{-3}
a_c	$\{5 \times 10^{-7}, 1.25 \times 10^{-6}, 2 \times 10^{-6}\}$	

Table 4.1: Several scenarios were computed for dark particle fraction decay Σ_χ , the particle decay rate Γ_χ , the velocity dispersion v_c and the phase transition scale factor a_c which are shown in the left column. In the middle column, we defined all values run for each parameter, and in the right column, we defined the numerical resolution Δ for every parameter simulated.

decaying DM fraction as a function of the particle lifetime for PIXIE sensitivity, allowing for μ and y distortion values of $\Sigma_\chi \approx 10^{-2}$ - 10^{-7} . In the next section we calculate SD for different choices of parameter for the energy injection parametrization presented in this section.

4.3 Spectral distortions from QCD dark matter

We aim now to determine the observational features of μ and y SD in the QCD dark matter scenario discussed in the previous section, whose features will soon be accessible to experiments. With this goal in mind, we compute the magnitudes of these SD associated with different choices of the main parameters of our model that were shown in table 4.1. The free parameters of our model are: the dark particle fraction decay Σ_χ , the particle decay rate Γ_χ , the velocity dispersion v_c , and the phase transition scale factor a_c . For the benchmark values of $a_c \in \{2 \times 10^{-6}, 1.25 \times 10^{-6}, 5 \times 10^{-7}\}$, we found the values of $\Gamma_{\text{crit}} \in \{0.37, 0.94, 5.89\} \text{ yr}^{-1}$ for ($v_c = 0.01$) and $\Gamma_{\text{crit}} \in \{0.43, 1.10, 6.88\} \text{ yr}^{-1}$ for ($v_c = 0.71$). We computed μ and y SD with eq.(3.18). First, we constrain μ and y for v_c and $\Gamma_\chi/\Gamma_{\text{crit}}$. We display these results in the heatmap scale on figure 4.4, for our three benchmark values $a_c = 2 \times 10^{-6}$ (left), 1.25×10^{-6} (middle) and 5×10^{-7} (right), and fixed $\Sigma_\chi = 5 \times 10^{-4}$ (for μ) and $\Sigma_\chi = 5 \times 10^{-3}$ (for y).

By inspecting the heatmap values in the figure 4.4, we note that μ and y SD are similar for every a_c chosen. For μ and y was discard $\Gamma_\chi/\Gamma_{\text{crit}} \lesssim 0.06$ (left), $\Gamma_\chi/\Gamma_{\text{crit}} \lesssim 0.02$ (middle), and $\Gamma_\chi/\Gamma_{\text{crit}} \lesssim 0.003$ (right). Approximately, for every v_c , we obtained the same μ and y distortion for each parameter $\Gamma_\chi/\Gamma_{\text{crit}}$ chosen in the range of $0 \lesssim v_c \lesssim 0.71$. We shade in gray the region in parameter $0.71 < v_c < 1$ and this region SD was obtained with a divergent behavior when

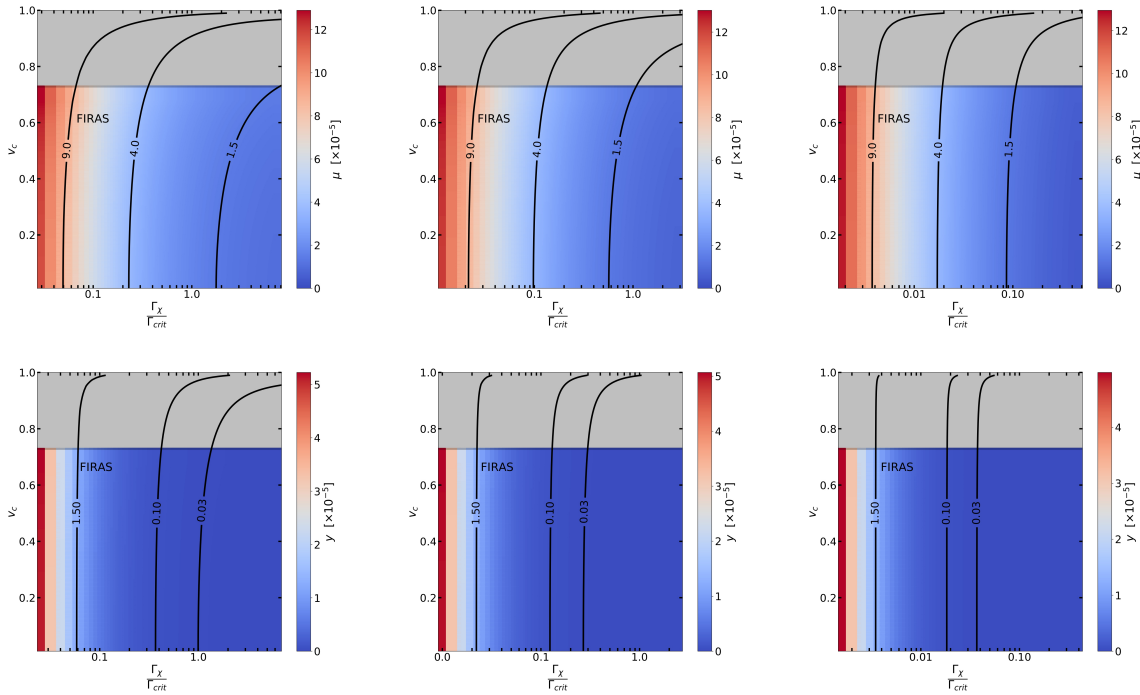


Figure 4.4: v_c -dependence of $\Gamma_\chi/\Gamma_{\text{crit}}$ on μ (top) and y (bottom) SD for different values of $a_c = 2 \times 10^{-6}$ (left), 1.25×10^{-6} (middle) and 5×10^{-7} (right). A smaller value of $\Gamma_\chi/\Gamma_{\text{crit}}$ yields a larger SD. Some of the μ and y SD values are marked along the dark lines. Results were obtained with $\Sigma_\chi = 5 \times 10^{-4}$ (for μ SD) and $\Sigma_\chi = 5 \times 10^{-3}$ (for y SD) fixed. We have used the values: $\mu_{\text{firas}} = 9 \times 10^{-5}$ and $y_{\text{firas}} = 1.5 \times 10^{-5}$.

v_c tends to 1.

In order to better appreciate the details of the SD and their dependence on Σ_χ , we now consider a modulation of the particle decay rate Γ_χ . We display the predictions for μ (left) and y (right) SD in the heatmap scale figure 4.5 for $a_c = 1.25 \times 10^{-6}$, for a corresponded $\Gamma_{\text{crit}} = 0.94$ and $v_c = 0.01$ fixed. The results show an interesting behavior of SD when Γ_χ is varied in the range $0.01 \leq \Gamma_\chi \leq 3.0$. For smaller $\Gamma_\chi/\Gamma_{\text{crit}}$, the larger the SD become for the Σ_χ considered. From figure 4.5, we have found (approximately) the window of Σ_χ that would be tested by PIXIE: $10^{-6} \lesssim \Sigma_\chi \lesssim 5 \times 10^{-4}$ for μ , and $10^{-6} \lesssim \Sigma_\chi \lesssim 5 \times 10^{-3}$ for y . Aiming at the detectability in the QCD dark matter scenario, in figure 4.6 is displayed the SD signal in the parameter space $v - \Delta I$ for $v_c \in \{0.01, 0.2, 0.5, 0.7\}$, $\Sigma_\chi \in \{10^{-4}, 10^{-5}, 10^{-6}\}$ and $\Gamma_\chi/\Gamma_{\text{crit}} \in \{1.06, 0.53, 3.18, 6.36\}$. We see that the signals obtained, lead to a SD signal larger than ΛCMD prediction, and it could be measured by PIXIE in the future.

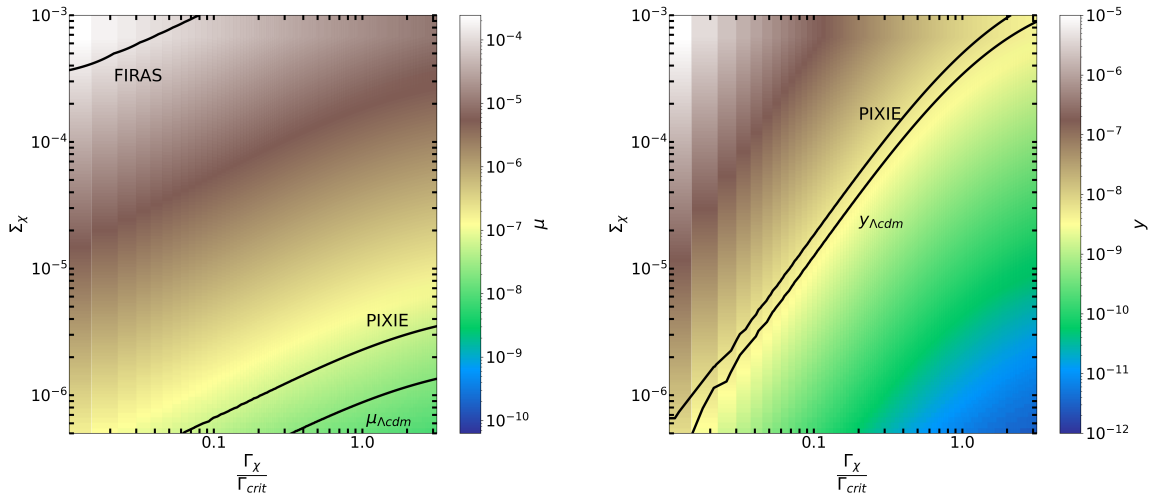


Figure 4.5: Σ_χ -dependence of $\Gamma_\chi/\Gamma_{\text{crit}}$ on μ (left) and y (right) SD. A larger value of Σ_χ yields a larger SD. In both cases, we have taken $a_c = 1.25 \times 10^{-6}$ with $\Gamma_{\text{crit}} = 0.94$. The μ , y sensibility from PIXIE values and ΛCDM signal were marked along the dark lines. We have used the values: $\mu_{\text{firas}} = 9 \times 10^{-5}$, $\mu_{\Lambda\text{cdm}} = 2 \times 10^{-8}$, $y_{\Lambda\text{cdm}} = 4.5 \times 10^{-9}$, $\mu_{\text{pixie}} = 5.2 \times 10^{-8}$ and $y_{\text{pixie}} = 6.6 \times 10^{-9}$.

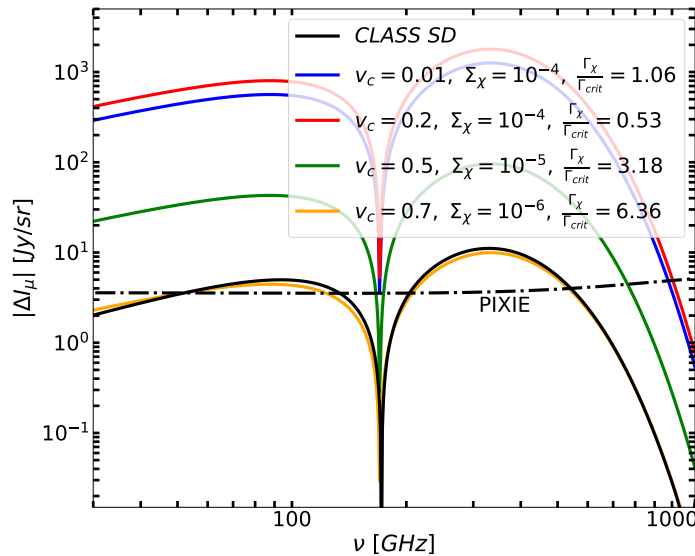


Figure 4.6: Predictions on the contribution to the distortion ΔI of the photon intensity eq.(3.17) arising from μ and y SD in the QCD dark scenario. Here has been plotted a several foretaste signals for different values of v_c , Σ_χ and $\Gamma_\chi/\Gamma_{\text{crit}}$. We have compared all signals obtained against the ΛCDM prediction gotten with the code CLASS.

Chapter 5

Spectral distortions from inflation

5.1 Axion monodromy model

Inflationary models based on axion monodromy [79; 80], on which we focus in this work, are motivated by the appearance in different scenarios of axions equipped with a low-energy potential that admits slow-roll over an extensive range in field space. For instance, in string compactifications, axions are particularly abundant [81]. They arise, e.g., from dualizing gauge fields over nontrivial cycles in the compact space of a string compactification or from integrating p -forms along p -cycles in type II strings.

Direct computations have shown that the canonically normalized fields associated with such axions exhibit in the large-field limit a monomial potential compatible with slow-roll [80; 82; 83]. These fields are super-Planckian but are naturally endowed with a sub-Planckian periodicity arising from an underlying shift symmetry. If worldsheet instantons or branes wrapping cycles are considered, this results in a small periodic modulation as a contribution to the low-energy effective potential of the axion [80]. Similarly, from a purely bottom-up perspective, axion monodromy can arise from a scenario where couplings between an axion and a gauge field strength yield a monomial potential [84] and gauge instantons produce the periodic modulation. Independently of its origin, besides providing a viable scope for large-field inflation, axion monodromy offers the appealing possibility of observable tensor modes [85]. The distinct features of axion monodromy further allow one to inspect other

possible observables for its signals in the cosmological history of our Universe.

In inflationary models based on axion monodromy, the potential energy of a canonically normalized axion ϕ can be written as

$$V(\phi) = V_0(\phi) + \Lambda^4 \cos\left(\frac{\phi}{f} + \gamma_0\right), \quad (5.1)$$

where γ_0 is a phase that is usually ignored (even though it naturally appears in this scenario and has an important impact on the value of n_s , as we discuss in section 5.4). Here, the amplitude of the periodic modulation is given by the scale Λ related to the strong dynamics that give rise to the potential, and f is the dimensionful decay parameter of the axion ϕ . In string constructions that support slow-roll inflation, it is known that in the large-field regime, the potential $V_0(\phi)$ can adopt the monomial structure [86; 87]

$$V_0(\phi) \approx \lambda^{4-p} \phi^p \quad \text{with } p < 2 \quad (5.2)$$

and a scale λ , which can be fixed by the amplitude \mathcal{A}_s of the scalar primordial fluctuations. Clearly, $V_0(\phi) \neq 0$ breaks the axion shift symmetry $\phi \rightarrow \phi + 2\pi f$ and induces a monodromy, as the potential changes after each period. The potential (5.1) has been shown to be useful to describe cosmological inflation, especially in scenarios with large tensor-to-scalar ratios [85] (where recent observations favor small over large powers, see section 5.4). In this case, since ϕ can interact during inflation with moduli before these achieve their stabilization, both the oscillation amplitude and the axion decay parameter vary in general, i.e. $\Lambda^4 = \Lambda^4(\phi)$ and $f = f(\phi)$. These dependencies induce a drift in the amplitude and in the oscillations, which may leave an imprint on cosmological observations. In some string models, the frequency drift can be expressed (at leading order in the slow-roll parameters) as [87]

$$f(\phi) = f_0 \left(\frac{\phi}{\phi_*}\right)^{-p_f}, \quad (5.3)$$

where f_0 is the standard axion decay constant, p_f is a drift parameter that encodes the dynamics of ϕ and moduli, and is adopted to be of order unity. Further, ϕ_* is the value of the field when

the pivot scale k_* exits the horizon, i.e. such that for a fixed k_* the relation $k_* = a(\phi_*)H(\phi_*)$ is satisfied. We focus here on the main signature of models with axion monodromy, which is the oscillatory behavior, considering that the periodic modulation is a small (nonperturbative) contribution. Hence, we ignore the drift in Λ and assume that the modulation depends on a small parameter $b \ll 1$ that relates Λ with the scale λ according to [88]

$$b := \frac{\Lambda^4}{V'_0(\phi_*)f(\phi_*)} = \frac{\Lambda^4}{\lambda^{4-p}p\phi_*^{p-1}f_0}. \quad (5.4)$$

With these ingredients, using perturbation theory, one can solve the background equation of motion for ϕ in the slow-roll regime and approximately linear potential, and then compute via the Mukhanov-Sasaki equation the primordial scalar power spectrum at leading order in b and in the limit¹ $f_0\phi_* \ll p$, ideal for observable non-Gaussianities [88]. The primordial scalar power spectrum reads [86; 87]

$$P_{\mathcal{R}}(k) = \mathcal{A}_s \left(\frac{k}{k_*}\right)^{n_s-1} \left\{ 1 + \delta n_s \cos \left[\frac{\phi_*}{f_0} \left(\frac{\phi_k}{\phi_*}\right)^{p_f+1} + \vartheta \right] \right\}, \quad (5.5)$$

where from slow-roll conditions is defined

$$\phi_k \approx \sqrt{2p \left(N_0 - \ln \left(\frac{k}{k_*} \right) \right)} \quad \text{with} \quad N_0 := N_* + \phi_{\text{end}}^2/2p. \quad (5.6)$$

Here, N_* is the number of e-folds fixed in the pivot scale², $\phi_{\text{end}} \approx p/\sqrt{2}$ corresponds to the value of the field at the end of slow-roll inflation. Thus, from eq.(5.6) we see that $\phi_* \approx \sqrt{2pN_0}$.

The amplitude of the oscillatory contribution to the power spectrum is given in this limit by

$$\delta n_s = 3b \sqrt{\frac{2\pi}{\alpha}} \quad \alpha := (p_f + 1) \frac{\phi_*}{2f_0N_0} \left(\frac{\sqrt{2pN_0}}{\phi_*} \right)^{p_f+1} \approx \frac{p(p_f + 1)}{f_0\phi_*}. \quad (5.7)$$

Note that small b and $f_0\phi_* \ll p$ implies $\delta n_s \ll 1$ too³. The amplitude of primordial power

¹Our units are such that the reduced Planck mass is the unity, $M_{\text{Pl}} = 1$.

²In this chapter we taken $N_{\text{tot}} \equiv N_*$, defined in eq.(2.55)

³this is an approximation from an exact analytic function shows in appendix B.2

p	ϕ_*	ϕ_{end}	$10^4\lambda$	n_s	r
$2/3$	8.77	0.47	14.4	0.977	0.046
1	10.75	0.71	5.85	0.974	0.069
$4/3$	12.42	0.94	1.78	0.971	0.092

Table 5.1: Approximate values of some parameters for our benchmark choices of p in inflationary models based on axion monodromy. We consider $k_* = 0.05 \text{ Mpc}^{-1}$ and $N_* = 57.5$. We take here the approximation $V \approx V_0 \sim \phi^p$. Both values for the inflaton field ϕ and the scale λ are given in units of M_{Pl} . For completeness, we provide n_s and r , which have been computed using eq.(5.9) in this approximation. The tension of these results against observable data is discussed in section 5.4.

spectrum is calculate with eq.(2.66), we find that in this limit

$$\mathcal{A}_s \approx \frac{V_0}{24\pi^2 \varepsilon_{V_0}} \Big|_{\phi=\phi_*} = \frac{\lambda^{4-p}}{12\pi^2 p^2} \phi_*^{p+2}, \quad (5.8)$$

which allows us to fit λ for different values of p by comparing with Planck's best fit value [40, table 1]. In table 5.1, we list the values of λ , ϕ_* and ϕ_{end} for three benchmark choices of p with fixed $k_* = 0.05 \text{ Mpc}^{-1}$ and $N_* = 57.5$. As we are interested in the compatibility with observations of inflation based on axion monodromy, it is useful to recall that for a model of inflation characterized by the potential $V(\phi)$, the values of the scalar tilt n_s and the tensor-to-scalar ratio r are respectively given in terms of the slow-roll parameters by

$$n_s = 1 - 6\varepsilon_V(\phi_*) + 2\eta_V(\phi_*) \quad \text{and} \quad r = 16\varepsilon_V(\phi_*), \quad (5.9)$$

where ε_V and η_V are defined in eq.(2.54).

5.2 Damping of primordial small-scale perturbations

In the epoch of radiation domination, energy stored in small-scale density perturbations is dissipated by the process Silk damping, this mechanism created spectral μ and y SD, this SD directly depends on the shape and amplitude of the primordial power spectrum of curvature perturbations, $P_{\mathcal{R}}(k)$. An analytic approximation for the effective rate of energy release arising

from the damping of adiabatic modes is given by (see [38] for details)

$$\frac{d(Q/\rho_\gamma)}{dz} = 2C^2 \int_{k_{\min}}^{\infty} \frac{k^4 dk}{2\pi^2} P_{\mathcal{R}}(k) \partial_z k_D^{-2} e^{-2k^2/k_D^2}. \quad (5.10)$$

Where $k_{\min} = 1 \text{ Mpc}^{-1}$ and k_D is diffusion scale given by [77]

$$k_D^{-2} = \int_z^{\infty} dz \frac{(1+z)}{6H(1+R)N_e\sigma_T} \left(\frac{R^2}{1+R} + \frac{16}{15} \right), \quad (5.11)$$

with $R = 3\rho_b/\rho_\gamma$ is the baryon-to-photon energy density ratio, and a good approximation of k_D is found in [38] as $k_D \approx 4.048 \times 10^{-6} (1+z)^{3/2} \text{ Mpc}^{-1}$. Note that the appearance of the primordial power spectrum $P_{\mathcal{R}}(k)$, as defined in eq.(2.62), emphasizes an unavoidable bond between SD and inflation, as the structure of $P_{\mathcal{R}}(k)$ is defined by the inflationary process. For adiabatic modes $C^2 \approx (1 + 4R_v/15)^{-2} \approx 0.813$ is a normalization coefficient with $4R_v/15$ accounting for the correction due to the anisotropic stress in the neutrino fluid. Inserting eq.(5.10) in eq.(3.18) and performing the integration over z , one arrives at a single integral expression for μ and y SD in the k -space [28]

$$\mu \approx \int_{k_{\min}}^{\infty} \frac{k^2 dk}{2\pi^2} P_{\mathcal{R}}(k) W^\mu(k), \quad (5.12a)$$

$$y \approx \int_{k_{\min}}^{\infty} \frac{k^2 dk}{2\pi^2} P_{\mathcal{R}}(k) W^y(k). \quad (5.12b)$$

Where $W^\mu(k)$ and $W^y(k)$ are the so-called k -space window functions for the respective SD, which account for the acoustic damping and thermalization effects, these are showed in appendix C.3.

The approximation in eqs.(5.12), is valid when the underlying model is similar to the concordance model, which applies in particular for models based on axion monodromy with parameters that comply with the constraints imposed by Planck data. Previous works have shown that SD can place robust bounds on the amplitude of the primordial power spectrum arising from various inflationary potentials (exhibiting peculiar features, such as bumps, kinks, and discontinuities) [25; 27; 28; 73]. In the following we focus on the study of the SD produced by inflationary models based on axion monodromy.

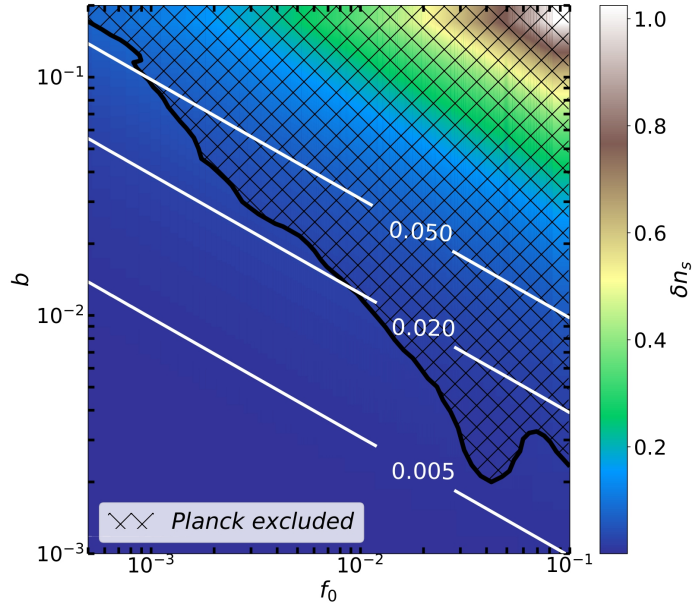


Figure 5.1: Constraints at 68% C.L. for the axion decay constant f_0 and the modulating parameter b for $p = 4/3$ based on Planck's data [70, fig. 32]. The shaded region has been excluded. The heatmap refers to values of δn_s associated with (b, f_0) according to eq.(5.7) with our choice of $p_f = -0.7$, $N_\star = 57.5$ and $\phi_\star = 12.38 M_{\text{Pl}}$. Some of the δn_s values are marked along the white lines.

5.3 Spectral distortions from axion monodromy

We aim now to determine the observational features of μ and y SD in the inflationary scenario based on axion monodromy discussed in section 5.1, whose features could soon be accessible to experiments. With this goal in mind, we compute the magnitudes of these SD associated with different choices of the main parameters of our model. The free parameters of our model are: the modulation b , the axion decay constant f_0 , the monomial power p , the oscillation drifting power p_f , and the phase ϑ , which we set to zero for simplicity. To compare with observations and previous results, we set the pivot scale to $k_\star = 0.05 \text{ Mpc}^{-1}$, and the number of e-folds at that scale to $N_\star = 57.5$, assuming instantaneous reheating. As discussed in section 5.1, ϕ_\star , ϕ_{end} and λ can be determined from the previous free parameters and the observed value of \mathcal{A}_s , and δn_s is calculated via eq.(5.7). For the benchmark values of $p \in \{2/3, 1, 4/3\}$, we find the values displayed in table 5.1. For different choices of the free parameters, we

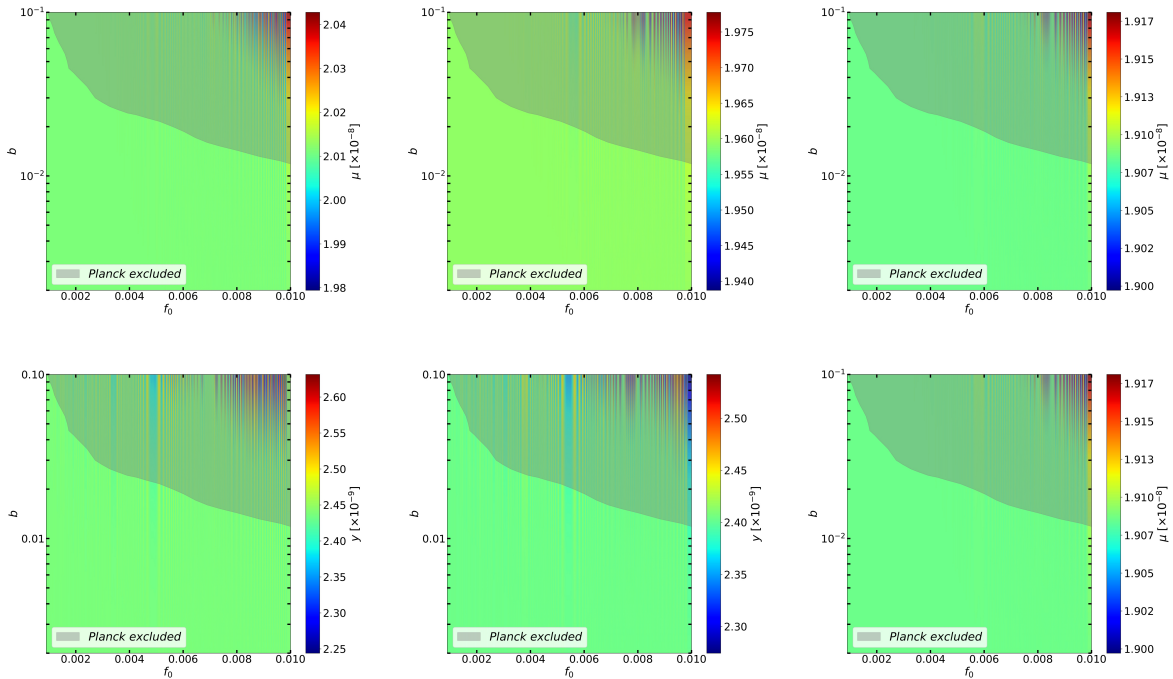


Figure 5.2: μ (top) and y (bottom) SD in axion-monodromy inflation, computed via eq.3.17 in the (b, f_0) parameter space. We explore here the region with $10^{-3} \leq b \leq 0.1$ and $9 \times 10^{-4} \leq f_0 \leq 0.01$. We take our three benchmark values $p = 2/3$ (left), 1 (middle), $p = 4/3$ (right), and fixed $p_f = -0.7$. The gray-shaded area corresponds to the region excluded by Planck at 68% C.L. as shown in figure 5.1.

compute μ and y SD, eq.(5.12), using the primordial power spectrum for axion monodromy, eq.(5.5). The parameter space that we explore is bounded to the following values

$$10^{-3} \leq b \leq 0.1, \quad 9 \times 10^{-4} \leq f_0 \leq 0.01, \quad \text{and} \quad -0.75 \leq p_f \leq 1.0. \quad (5.13)$$

We adopt these values because they favor sizable SD while complying with all our priors. In addition, as we will shortly discuss, this selection is found within the parameter window explored by Planck. To achieve compatibility with observations we subject the parameters to the bounds set by the Planck collaboration [70, section 7.4]. Planck established limits on f_0 , p_f and δn_s in axion monodromy models with $p \in \{2/3, 1, 4/3\}$. We translate through the relation eq.(5.7) the bounds of f_0 and δn_s to constraints on f_0 as function of the modulation parameter b , for fixed p and p_f . Taking $p = 4/3$ and $p_f = -0.7$ to maximize these bounds, we show in figure 5.1 the (b, f_0) region of parameter space that is consistent with Planck data at

	$p = 2/3$	$p = 1$	$p = 4/3$
$10^8 \mu$	2.011	1.956	1.908
$10^9 y$	2.438	2.404	2.371

Table 5.2: Dominant predicted values of μ and y SD by inflationary models with axion monodromy for a choice monomial powers p and fixed $p_f = -0.7$.

68% C.L. We see that the admissible values lead to small δn_s , which justifies the blue color in the heatmap scale. From [70, figure 32], we read off that the values of p_f in our parameter space eq.(5.13) are all allowed if the combination of (b, f_0) is chosen to comply with figure 5.1. The constraints for $p = 2/3$ and 1 are similar but somewhat milder [70]. Hence, using the restrictions of figure 5.1 for all our choices of p leads to a conservative scenario, where results based on these constraints are compatible with observations. In figure 5.2 we display the predictions of inflationary models based on axion monodromy for μ (top) and y (bottom) SD as functions of the modulation amplitude b and the axion decay constant f_0 , for fixed $p_f = -0.7$ and different values of $p = 2/3$ (left), 1 (middle) and $4/3$ (right). We fix $p_f = -0.7$ because this value delivers the largest SD, as we shall shortly see. We shade in gray the region in parameter space excluded by Planck, according to the bounds presented in figure 5.1. The predominantly predicted values of SD (appearing in green) are given in table 5.2. By inspecting the heatmap values in the figure, we note that arbitrary b and f_0 only lead to SD values that differ by up to 1% with respect to the dominant predictions.

Based on the results displayed in figure 5.2, in order to better appreciate the details of the SD and their dependence on p_f , we consider now a choice of the axion decay constant f_0 and the modulation parameter b and vary p_f . We present our results in figure 5.3 for $f_0 = 0.01$. The results show an interesting wave-damping behavior for the benchmark values of the monomial power $p = 2/3$ (left panel), 1 (center panel) and $p = 4/3$ (right panel). For our selected value of f_0 we take the maximally allowed value $b = 0.01$ (blue for μ and green for y SD) and the minimally explored value $b = 5 \times 10^{-4}$ (red for μ and magenta for y SD). As expected from eq.(5.5), smaller values of b lead to smaller SD. Note that the smaller p_f is, the larger the SD become. The central value (horizontal dashed line) represents the magnitude of the SD for a standard power-law potential with $b = 0$ for each value of p . In average, for $p_f = -0.7$ the SD are 0.2% for μ and 0.7% for y larger than in the standard $b = 0$ case. The oscillatory

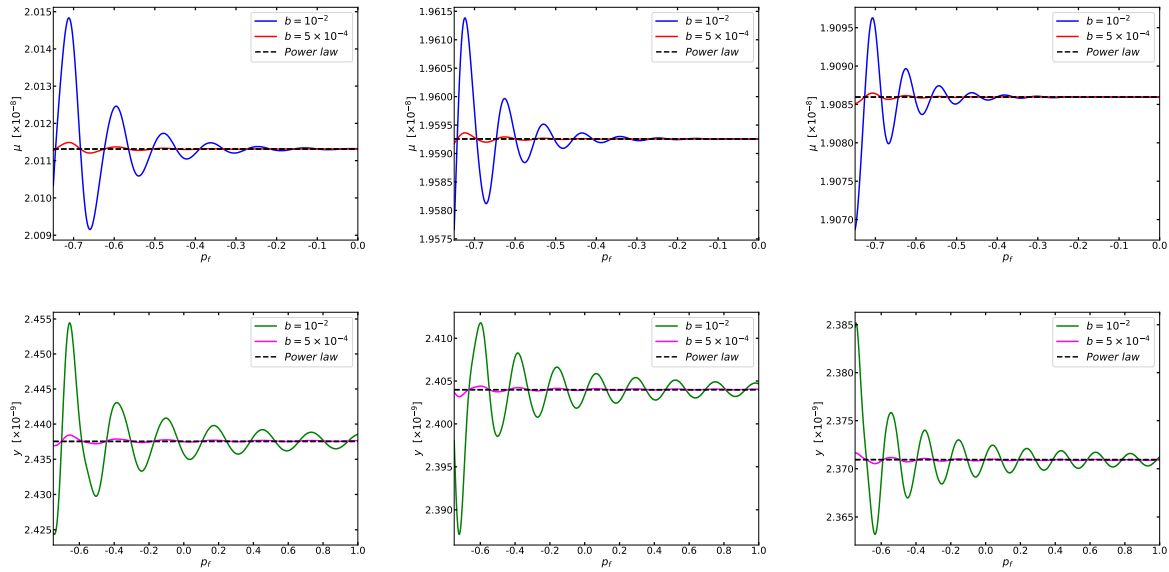


Figure 5.3: p_f -dependence of μ (top) and y (bottom) SD in models based on axion monodromy for different values of p : $p = 2/3$ (left), $p = 1$ (middle) and $p = 4/3$ (right). A larger value of the modulation parameter b yields larger SD, cf. eq.(5.5). As p_f grows, the oscillatory behavior of SD in axion-monodromy models tends to the values of a standard power-law potential with $b = 0$. We assume here a fixed axion decay constant, $f_0 = 0.01$.

behavior of SD in axion monodromy tends to the central value for larger positive values of the drifting power p_f . Recalling that this parameter encodes the possible interactions between the inflation axion and background moduli fields (or similar) of the full model if some dynamics among such fields is left, variations of p_f could happen and, hence the oscillatory behavior displayed in figure 5.3 might be observable.

Let us now include the variation of the axion decay constant f_0 in the scheme. We show in figure 5.4 all predicted values of μ and y SD by axion-monodromy models. As before, we display on the top panels the values of the μ SD and in the bottom the values for y . Further, from left to right, we show the results for $p = 2/3, 1$ and $4/3$. The heatmap allows us to appreciate the effect on the SD of the variation of p_f . An interesting observation is that choosing $p_f \approx 1$ or small values of f_0 lead to SD values that coincide with the central value obtained from a standard power-law potential (with $b = 0$). This implies a conservative theoretical bound for detection of SD due to axion monodromy, distinguishable from power law, at around $f_0 \gtrsim 4 \times 10^{-3}$ and $p_f \lesssim 0.2$. Note that there are deviations from the central value of y SD for smaller f_0 ; however, y SD are in general an order of magnitude smaller than μ SD and hence leave a much

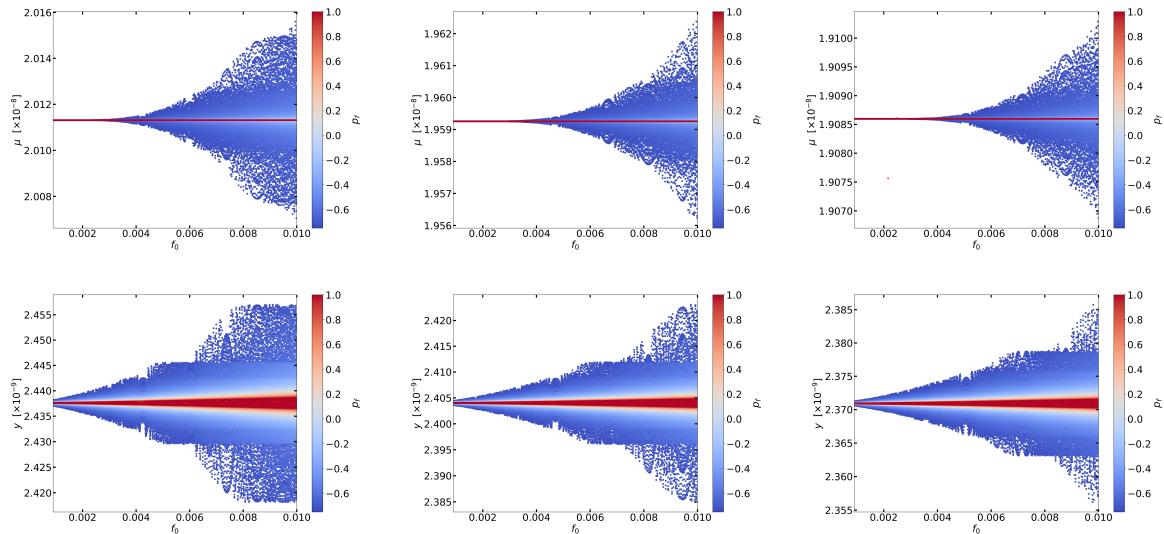


Figure 5.4: Values of μ (top) and y (bottom) SD as functions of the axion decay constant f_0 and the frequency drift p_f in inflationary models based on axion monodromy. We have set the modulation parameter $b = 0.01$ and display the results for $p = 2/3$ (left), $p = 1$ (middle) and $p = 4/3$ (right). For smaller values of f_0 and/or values of p_f close to unity, the results from axion monodromy and standard power law with $V \sim \phi^p$ are very similar.

p	axion-monodromy SD		power-law SD	
	$10^8 \max(\mu)$	$10^9 \max(y)$	$10^8 \mu$	$10^9 y$
$2/3$	2.0148	2.4545	2.0113	2.4376
1	1.9614	2.4118	1.9592	2.4039
$4/3$	1.9096	2.3852	1.9085	2.3708

Table 5.3: Comparison between the maximal values of SD in axion monodromy (with $b = 0.01$) and power-law inflationary models ($b = 0$). The maximal values of μ SD occur at $p_f = \{-0.71, -0.72, -0.71\}$ and of y at $p_f = \{-0.66, -0.59, -0.74\}$, for $p \in \{2/3, 1, 4/3\}$, respectively. In all cases, we have taken $f_0 = 0.01$ and $b = 0.01$.

weaker imprint in the SD signals. Aiming at the detectability of our scenario, we focus on the parameter values that produce the largest SD signals and are compatible with Planck data. By inspecting figure 5.2, 5.3 and 5.4, we realize that $b = 0.01 = f_0$ and $p_f \approx -0.7$ render the most sizable signals. For each benchmark p value, we show the resulting maximal values of μ and y SD in table 5.3. To establish a comparison with the standard power-law case ($b = 0$), we also present in the table the SD values for all p values. We find small but important enhancements of about $0.2 - 0.7\%$ in axion monodromy over the standard power-law scenario. To conclude this section, we now address the question of whether the SD predictions associated with inflationary models based on axion monodromy can be falsified by future observational

data. With this goal in mind, first we compute the μ and y contributions to the distortions of the photon intensity spectrum $\Delta I(\nu)$, see eq.(3.17), and compare the results to the sensitivity of the PIXIE experiment and its enhanced version Super-PIXIE. In figure 5.5 we plot in the left the intensity in units of $\text{Jy/sr} = 10^{-26} \text{W m}^{-2} \text{Hz}^{-1} \text{sr}^{-1}$ for axion monodromy with $p = 2/3$ (red dash-dotted curve), $p = 1$ (blue dotted), $p = 4/3$ (magenta dashed curve), and for the ΛCDM model (black continuous curve). The latter is obtained from inserting the observed values of $n_s = 0.96605 \pm 0.0042$ [40, Table 1] and \mathcal{A}_s in the standard primordial power spectrum, eq.(2.62), with $\alpha_s = 0$ and then computing the SD as in eq.(5.12). We observe that in the range $55 \lesssim \nu \lesssim 110$ GHz axion monodromy would leave an observable SD signal whereas SD from ΛCDM would not be detectable. Moreover, to quantify the difference between SD from axion monodromy (am) and from ΛCDM , we compute $|\Delta I_{\Lambda\text{CDM}} - \Delta I_{\text{am}}|$ and express this difference on the right-hand side of figure 5.5 as a percentage of the ΛCDM result. We see that they can differ by up to about 10% in the physically relevant region, $\nu \lesssim 100$ GHz and $\nu \gtrsim 250$ GHz. Interestingly, the greatest discrepancy, though marginal, is realized for axion monodromy with $p = 2/3$.

A second important observation we need to study the falsifiability of axion monodromy is the experimental error of future measurements of SD. As mentioned earlier, the expected standard error of Super-PIXIE is given by $\sigma(\mu) \simeq 7.7 \times 10^{-9}$ and $\sigma(y) \simeq 1.6 \times 10^{-9}$ [32; 37]. Unfortunately, our comparison in table 5.3 between power-law and axion monodromy indicates that we need $\sigma(\mu), \sigma(y) \sim 10^{-11}$ to distinguish between those two scenarios. This can be achieved by the proposed configurations of PIXIE that shall enhance its sensitivity by a factor of 100 [38].

5.4 Planck constraints on n_s and r

Since axion monodromy is known to yield large tensor modes, current bounds on the spectral tilt n_s and the tensor-to-scalar ratio r are additional observables that can be used to falsify inflationary models based on axion monodromy. In this section, we briefly revise the status of the model on this topic. The latest Planck's best-fit value for the spectral tilt is $n_s = 0.96605 \pm 0.0042$ [40, Table 1], while the upper bound on the tensor-to-scalar ratio is

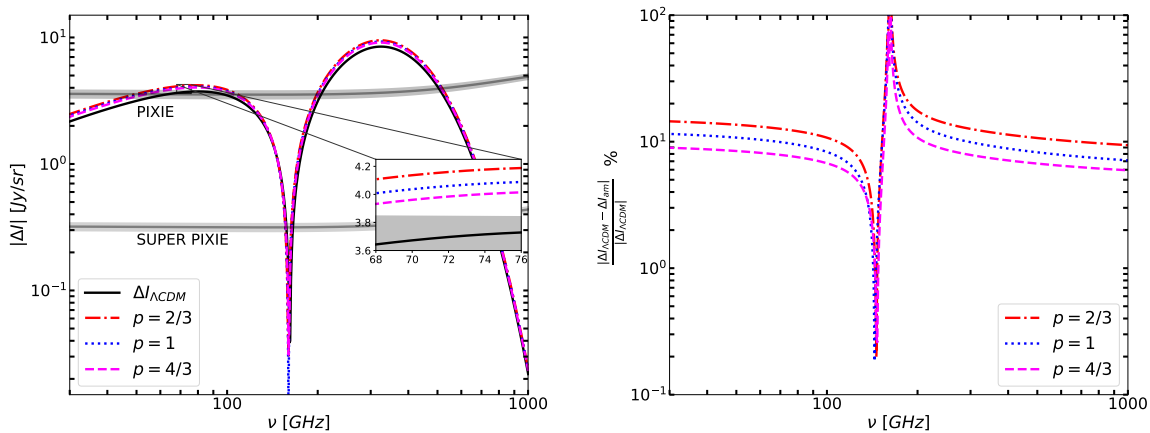


Figure 5.5: Predictions on the contribution to the distortion ΔI of the photon intensity eq.(3.17) arising from μ and y SD in axion monodromy inflationary models, contrasted against the Λ CDM prediction. To explore the maximal size of the SD contributions from axion monodromy complying with Planck bounds, we take $p_f = -0.7$, $b = 0.01$ and $f_0 = 0.01$. In the left, we display the three curves described for the benchmark values of monomial power, $p = 2/3$ (red dash-dotted curve), $p = 1$ (blue dotted) and $p = 4/3$ (magenta dashed), and the Λ CDM prediction (black continuous curve). We further show the sensitivity of future PIXIE and Super PIXIE missions (curves adapted from [32, figure 9]). In the right, we evaluate the difference between the axion-monodromy ΔI_{am} and Λ CDM $\Delta I_{\Lambda\text{CDM}}$ predicted intensities for the different benchmark p values. For frequencies outside the range $100\text{GHz} \lesssim \nu \lesssim 250\text{GHz}$ the difference w.r.t. the fiducial signal is about 10%.

p	γ_0	ϕ_*	ϕ_{end}	$10^4 \lambda$	n_s	r
$2/3$	2.00	8.78	0.67	14.38	0.965	0.046
1	2.78	10.77	0.99	5.85	0.965	0.069
$4/3$	4.54	12.38	0.01	1.79	0.965	0.093

Table 5.4: Improved parameters of axion-monodromy inflation with fixed values of $b = f_0 = 0.01$, $p_f = -0.7$, $k_* = 0.05 \text{ Mpc}^{-1}$ and $N_* = 57.5$. Both the inflaton field ϕ and the scale λ are given in units of Planck mass. By varying the value of the phase γ_0 (in radians) in eq.(5.1), it is possible to successfully fit the spectral tilt n_s while keeping the tensor-to-scalar ratio r within the 3σ C.L. observed region, cf. table 5.1.

about $r < 0.123$ at 2σ based only on Planck's TT,TE,EE+lowE+lensing data [40] (depicted by the green contours of figure 5.6), and $r < 0.048$ at 3σ C.L. based on the latest combination of Planck's data together with BICEP/Keck (BK18) and BAO data [61] (depicted by the blue contours in figure 5.6). Disregarding the periodic modulation of axion monodromy, from eq.(5.9) we find that the resulting single-field monomial potential yields

$$n_s \approx 1 - (p+2)/2N_0 \quad \text{and} \quad r \approx 4p/N_0. \quad (5.14)$$

In this scenario, we note some (known) tension between the prediction of a model based on $V \sim \phi^p$ and the observations. The values of n_s and r for our benchmark values of N_\star and $p \in \{2/3, 1, 4/3\}$ are presented in table 5.1. In the left plot of figure 5.6 we explore these results for other admissible values of e-folds⁴ N_\star . The dumbbells in different colors illustrate the values predicted by such simplified model with three different values of p . The small (large) bullet corresponds to $N_\star = 50$ ($N_\star = 60$) e-folds and the star denotes our (arbitrarily chosen) benchmark value $N_\star = 57.5$, which is frequently used in the literature. In this approximated model, n_s is found within the 3σ region of the combined fit of Planck and BK18. However, although r is within the 2σ region of Planck's data, it lies beyond the 3σ C.L. region of the latest combined data.

So far, we have set $b = 0$ and hence ignored the oscillatory modulation of axion monodromy. Setting the small modulation parameter $b \neq 0$ introduces important changes on the predictions for n_s and r . First, ϕ_\star , ϕ_{end} and N_\star depend on b, f_0, γ_0 and p_f besides p and can only be computed numerically using an iterative approach. For fixed values of p, b, f_0, γ_0 and p_f , the value of ϕ_\star has an oscillatory behavior. Consequently, also the values of n_s and r oscillate. The spectral tilt oscillates in a wide range of values while N_\star varies a little, depending on p and the angle γ_0 appearing in the potential eq.(5.1). The tensor-to-scalar ratio, on the other hand, oscillates minimally, such that its value resembles the standard power-law result, which only depends on p and N_\star . Interestingly, these properties pull n_s and r closer to the observed values. In the right plot of figure 5.6, we display all different values of n_s and r for $50 \leq N_\star \leq 60$ and our three benchmark choices of $p \in \{2/3, 1, 4/3\}$, assuming fixed values⁵ of $b = f_0 = 0.01$ and $p_f = -0.7$. The phase γ_0 has been chosen independently for each p with the goal of best fitting n_s at $N_\star = 57.5$ to the observed value; the stars in the plot correspond to the values of n_s and r that we obtain for $p = 4/3$ (top), 1 (middle) and $2/3$ (bottom). We conclude that $p \leq 2/3$ and nontrivial phases γ_0 lead to axion monodromy models compatible with current Planck observations at 1σ , and at 3σ for Planck and BICEP/Keck 18 combined data.

⁴Note that various values of N_\star can be associated with $k_\star = 0.05 \text{ Mpc}^{-1}$ because N_\star depends on many other (undetermined) parameters, see e.g. [89, eq. (3.11)].

⁵The values of b, f_0, p_f are chosen to maximize the spectral distortions of the model, as we saw in section 5.3.

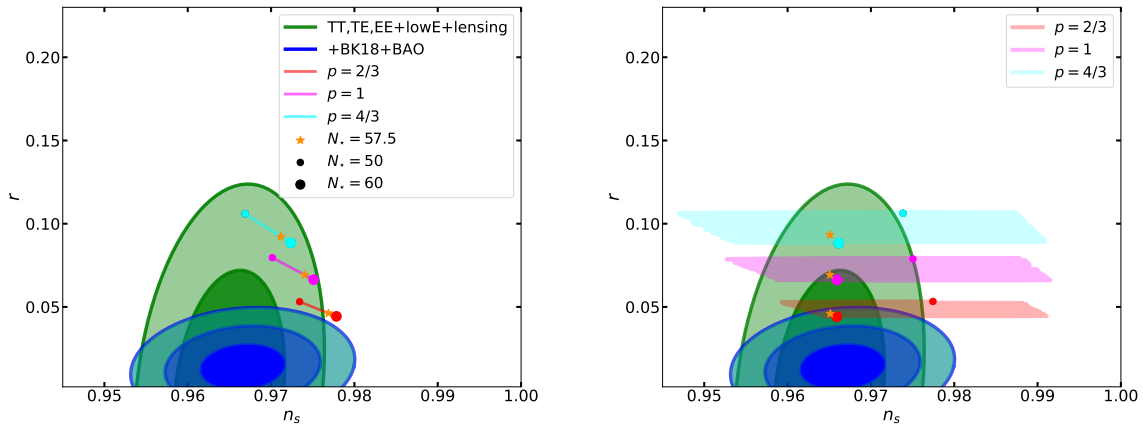


Figure 5.6: Predictions for n_s and r from ϕ^p (left) and axion monodromy inflation (right) with $50 \leq N_* \leq 60$ e-folds contrasted against the observational constraints from the CMB Planck data in combination with baryon acoustic oscillation (BAO), CMB lensing data and BICEP/Keck data. The (higher) green contours correspond to the 1σ and 2σ C.L. regions based on Planck’s CMB data (TT,TE,EE+lowE) and lensing [40]. The (lower) blue contours depict the 1σ , 2σ and 3σ C.L. regions resulting from combining the previous data with BICEP/Keck 18 (BK18) and BAO data [61]. For axion monodromy (right), we used the values of $\gamma_0 = 2.00$ ($p = 2/3$), 2.78 ($p = 1$) and 4.54 ($p = 4/3$) in radians, which produce the best fit for n_s at $N_* = 57.5$. Labels on the right panel are the as in the left one.

Chapter 6

Summary and Conclusions

The Λ CDM is the concordance model of Cosmology and is in agreement with most of the astrophysical and cosmological observations. However, we have presented in chapter 2, the challenges that the CDM model needs to explain: first, the number of satellite galaxies around the milky way is smaller than expected from Λ CDM numerical simulations. Second, the model predicts steeply cuspy density profiles, causing a large fraction of haloes to survive as substructures inside larger haloes; both of these problems can be alleviated with a dark matter model whose nature at early stages suppresses large-scale structure formation.

The inflationary paradigm is well-motivated because it provides a solution to the horizon and flatness problems inherent to the Hot Big Bang cosmology. To test inflation, CMB SD has demonstrated that it will be an important tool for upcoming observational probes.

The unprecedented precision of the forthcoming SD experiment naturally invites forecasting and constrains dark matter and inflationary models. In this thesis, we have computed the signal of CMB SD in two different scenarios: QCD dark matter and axion monodromy inflation. For both scenarios, we have presented the main equation for the parametrization of the energy injection rates related, determined the observational features of μ and y SD, and presented the main results in chapters 4 and 5.

In the QCD dark matter, results show an interesting behavior of the SD when Γ_χ was varied in the range $0.01 \leq \Gamma_\chi \leq 3.0$. Figure 4.4 depicts that the smaller $\Gamma_\chi/\Gamma_{\text{crit}}$, the maximum values were obtained for the benchmark values of Σ_χ . Figure 4.5 shows the μ (left) and y (right) distortions computed value when the parameter space for the scale factor a_c is explored

with a marginalized $v_c = 0.01$. We have constraint the value of Σ_χ in the range $0.01 \leq \Gamma_\chi \leq 3.0$, for smaller $\Gamma_\chi/\Gamma_{\text{crit}}$, that could be observationally constrained by PIXIE: $10^{-6} \lesssim \Sigma_\chi \lesssim 5 \times 10^{-4}$ for μ and $10^{-6} \lesssim \Sigma_\chi \lesssim 5 \times 10^{-3}$ for y distortions. The detectability of the QCD dark matter scenario is shown in figure 4.6, in the parameter space $v - \Delta I$ for $v_c \in \{0.01, 0.2, 0.5, 0.7\}$, $\Sigma_\chi \in \{10^{-4}, 10^{-5}, 10^{-6}\}$ and $\Gamma_\chi/\Gamma_{\text{crit}} \in \{1.06, 0.53, 3.18, 6.36\}$. This last plot shows that several scenarios of QCD dark matter considered in this work may be tested in the future.

On the other hand, for axion monodromy inflation, we identified in section 5.3 some values that maximize the resulting distortions for some benchmark models (with the powers $p \in \{2/3, 1, 4/3\}$ of the monomial contribution to the inflationary potential), see tables 5.3 and 5.4. The main results are displayed in figures 5.2–5.5. Interestingly, accepting the possibility of a drifting axion decay parameter p_f that varies during inflation, the resulting distortions exhibit a wave-damping behavior, which may be observable. If the drifting does not vary and develops a value $p_f \lesssim -0.7$, the associated SD become sizable. Beyond this feature, we find that the distortions arising from axion monodromy are distinguishable from the most conservative SD signal based on current Λ CDM observations, with up to 10% deviations with respect to standard values in the observable frequency window, cf. figure 5.5.

On a less positive note, we find it challenging for future missions, such as PIXIE and Super PIXIE, to discriminate between inflationary models based on a power-law potential and axion monodromy. SD in axion monodromy with $f_0 \gtrsim 4 \times 10^{-3}$ and $p_f \lesssim 0.2$ differ maximally from the signal of a standard scenario based on a power-law potential. However, the difference is just of order 1% or less. Consequently, one needs greater experimental accuracy than currently achievable to notice such small discrepancies. We expect that this caveat shall be solved by PIXIE setups capable of improving the sensitivity by at least 100 times, such as those already proposed in [38].

A fully updated analysis of the SD in addition to other astrophysical and cosmological signals from these models must be carried out. The current work represents a step towards this goal. It would be interesting to also include extensions to the scenario studied here.

Bibliography

- [1] D. Baumann, *Cosmology*. Cambridge University Press, 7 2022.
- [2] A. G. Riess *et al.*, “Observational evidence from supernovae for an accelerating universe and a cosmological constant,” *Astron. J.*, vol. 116, pp. 1009–1038, 1998.
- [3] S. Perlmutter *et al.*, “Measurements of Omega and Lambda from 42 high redshift supernovae,” *Astrophys. J.*, vol. 517, pp. 565–586, 1999.
- [4] Planck Collaboration and e. a. Aghanim, N., “Planck 2018 results. VI. Cosmological parameters,” *ArXiv e-prints*, July 2018.
- [5] S. Alam *et al.*, “The Completed SDSS-IV extended Baryon Oscillation Spectroscopic Survey: Cosmological Implications from two Decades of Spectroscopic Surveys at the Apache Point observatory,” 7 2020.
- [6] R. Ahumada *et al.*, “The Sixteenth Data Release of the Sloan Digital Sky Surveys: First Release from the APOGEE-2 Southern Survey and Full Release of eBOSS Spectra,” 12 2019.
- [7] A. Aghamousa *et al.*, “The DESI Experiment Part I: Science, Targeting, and Survey Design,” 2016.
- [8] LSST Science Collaboration, P. A. Abell, J. Allison, S. F. Anderson, J. R. Andrew, J. R. P. Angel, L. Armus, D. Arnett, S. J. Asztalos, T. S. Axelrod, and et al., “Lsst science book, version 2.0,” *arXiv*, vol. abs/0912.0201, 2009.
- [9] R. Laureijs, J. Amiaux, S. Arduini, J. Auguères, J. Brinchmann, R. Cole, M. Cropper,

- C. Dabin, L. Duvet, A. Ealet, *et al.*, “Euclid definition study report. arxiv 2011,” *arXiv preprint arXiv:1110.3193*, 2011.
- [10] J. T. de Jong, G. A. V. Kleijn, K. H. Kuijken, E. A. Valentijn, *et al.*, “The kilo-degree survey,” *Experimental Astronomy*, vol. 35, no. 1-2, pp. 25–44, 2013.
- [11] D. Scolnic *et al.*, “The Complete Light-curve Sample of Spectroscopically Confirmed SNe Ia from Pan-STARRS1 and Cosmological Constraints from the Combined Pantheon Sample,” *Astrophys. J.*, vol. 859, no. 2, p. 101, 2018.
- [12] T. S. V. Albada, R. Sancisi, M. Petrou, and R. J. Tayler, “Dark Matter in Spiral Galaxies [and Discussion],” *Phil. Trans. Roy. Soc. Lond. A*, vol. 320, no. 1556, pp. 447–464, 1986.
- [13] M. López-Corredoira, “Tests and problems of the standard model in Cosmology,” *Found. Phys.*, vol. 47, no. 6, pp. 711–768, 2017.
- [14] J. R. Ellis and D. V. Nanopoulos, “Beyond the standard model of cosmology,” *AIP Conf. Proc.*, vol. 743, no. 1, pp. 450–456, 2004.
- [15] J. F. Navarro, C. S. Frenk, and S. D. M. White, “A Universal density profile from hierarchical clustering,” *Astrophys. J.*, vol. 490, pp. 493–508, 1997.
- [16] J. Chluba, “Which spectral distortions does Λ CDM actually predict?,” *Mon. Not. Roy. Astron. Soc.*, vol. 460, no. 1, pp. 227–239, 2016.
- [17] J. Silk, “Cosmic black body radiation and galaxy formation,” *Astrophys. J.*, vol. 151, pp. 459–471, 1968.
- [18] R. A. Daly, “Spectral Distortions of the Microwave Background Radiation Resulting from the Damping of Pressure Waves,” *Astrophys. J.*, vol. 371, p. 14, Apr. 1991.
- [19] J. D. Barrow and P. Coles, “Primordial density fluctuations and the microwave background spectrum,” *Mon. Not. Roy. Astron. Soc.*, vol. 248, pp. 52–57, Jan. 1991.
- [20] W. Hu, D. Scott, and J. Silk, “Power spectrum constraints from spectral distortions in the cosmic microwave background,” *Astrophys. J. Lett.*, vol. 430, pp. L5–L8, 1994.

- [21] G. Cabass, A. Melchiorri, and E. Pajer, “ μ distortions or running: A guaranteed discovery from CMB spectrometry,” *Phys. Rev. D*, vol. 93, no. 8, p. 083515, 2016.
- [22] Y. B. Zel’dovich, A. F. Illarionov, and R. A. Sunyaev, “The Effect of Energy Release on the Emission Spectrum in a Hot Universe,” *Soviet Journal of Experimental and Theoretical Physics*, vol. 35, p. 643, Jan. 1972.
- [23] J. Chluba and R. A. Sunyaev, “Superposition of blackbodies and the dipole anisotropy: A Possibility to calibrate CMB experiments,” *Astron. Astrophys.*, vol. 424, pp. 389–408, 2003.
- [24] Y. B. Zeldovich and R. A. Sunyaev, “The Interaction of Matter and Radiation in a Hot-Model Universe,” *Astrophys. Space Sci.*, vol. 4, pp. 301–316, July 1969.
- [25] J. Chluba, R. Khatri, and R. A. Sunyaev, “CMB at 2x2 order: The dissipation of primordial acoustic waves and the observable part of the associated energy release,” *Mon. Not. Roy. Astron. Soc.*, vol. 425, pp. 1129–1169, 2012.
- [26] R. Khatri and R. A. Sunyaev, “Creation of the CMB spectrum: precise analytic solutions for the blackbody photosphere,” *JCAP*, vol. 06, p. 038, 2012.
- [27] J. Chluba, “Distinguishing different scenarios of early energy release with spectral distortions of the cosmic microwave background,” *Mon. Not. Roy. Astron. Soc.*, vol. 436, pp. 2232–2243, 2013.
- [28] J. Chluba and D. Grin, “CMB spectral distortions from small-scale isocurvature fluctuations,” *Mon. Not. Roy. Astron. Soc.*, vol. 434, pp. 1619–1635, 2013.
- [29] J. Chluba *et al.*, “Spectral Distortions of the CMB as a Probe of Inflation, Recombination, Structure Formation and Particle Physics: Astro2020 Science White Paper,” *Bull. Am. Astron. Soc.*, vol. 51, no. 3, p. 184, 2019.
- [30] J. A. Rubino-Martin, J. Chluba, and R. A. Sunyaev, “Lines in the Cosmic Microwave Background Spectrum from the Epoch of Cosmological Hydrogen Recombination,” *Mon. Not. Roy. Astron. Soc.*, vol. 371, pp. 1939–1952, 2006.

- [31] J. A. D. Diacoumis and Y. Y. Y. Wong, “Using CMB spectral distortions to distinguish between dark matter solutions to the small-scale crisis,” *JCAP*, vol. 09, p. 011, 2017.
- [32] J. Chluba *et al.*, “New horizons in cosmology with spectral distortions of the cosmic microwave background,” *Exper. Astron.*, vol. 51, no. 3, pp. 1515–1554, 2021.
- [33] J. Chluba and D. Jeong, “Teasing bits of information out of the CMB energy spectrum,” *Mon. Not. Roy. Astron. Soc.*, vol. 438, no. 3, pp. 2065–2082, 2014.
- [34] M. Lucca, N. Schöneberg, D. C. Hooper, J. Lesgourgues, and J. Chluba, “The synergy between CMB spectral distortions and anisotropies,” *JCAP*, vol. 02, p. 026, 2020.
- [35] D. J. Fixsen, E. S. Cheng, J. M. Gales, J. C. Mather, R. A. Shafer, and E. L. Wright, “The Cosmic Microwave Background spectrum from the full COBE FIRAS data set,” *Astrophys. J.*, vol. 473, p. 576, 1996.
- [36] A. Kogut *et al.*, “The Primordial Inflation Explorer (PIXIE): A Nulling Polarimeter for Cosmic Microwave Background Observations,” *JCAP*, vol. 07, p. 025, 2011.
- [37] J. Delabrouille *et al.*, “Microwave spectro-polarimetry of matter and radiation across space and time,” *Exper. Astron.*, vol. 51, no. 3, pp. 1471–1514, 2021.
- [38] H. Fu, M. Lucca, S. Galli, E. S. Battistelli, D. C. Hooper, J. Lessgourgues, and N. Schöneberg, “Unlocking the synergy between CMB spectral distortions and anisotropies,” *JCAP*, vol. 12, no. 12, p. 050, 2021.
- [39] S. Dodelson, *Modern Cosmology*. Amsterdam: Academic Press, 2003.
- [40] N. Aghanim *et al.*, “Planck 2018 results. VI. Cosmological parameters,” *Astron. Astrophys.*, vol. 641, p. A6, 2020. [Erratum: *Astron. Astrophys.* 652, C4 (2021)].
- [41] P. Coles and F. Lucchin, *Cosmology: The Origin and evolution of cosmic structure*. 1995.
- [42] J. Lesgourgues, “The Cosmic Linear Anisotropy Solving System (CLASS) I: Overview,” 4 2011.

- [43] A. Arbey and F. Mahmoudi, “Dark matter and the early Universe: a review,” *Prog. Part. Nucl. Phys.*, vol. 119, p. 103865, 2021.
- [44] J. Silk *et al.*, *Particle Dark Matter: Observations, Models and Searches*. Cambridge: Cambridge Univ. Press, 2010.
- [45] J. Mastache and A. de la Macorra, “Bound Dark Matter (BDM) towards solving the small scale structure problem,” *JCAP*, vol. 03, p. 025, 2020.
- [46] J. S. Bullock and M. Boylan-Kolchin, “Small-Scale Challenges to the Λ CDM Paradigm,” *Ann. Rev. Astron. Astrophys.*, vol. 55, pp. 343–387, 2017.
- [47] A. Albrecht and P. J. Steinhardt, “Cosmology for Grand Unified Theories with Radiatively Induced Symmetry Breaking,” *Phys. Rev. Lett.*, vol. 48, pp. 1220–1223, 1982.
- [48] A. H. Guth, “The Inflationary Universe: A Possible Solution to the Horizon and Flatness Problems,” *Phys. Rev. D*, vol. 23, pp. 347–356, 1981.
- [49] A. D. Linde, “A New Inflationary Universe Scenario: A Possible Solution of the Horizon, Flatness, Homogeneity, Isotropy and Primordial Monopole Problems,” *Phys. Lett. B*, vol. 108, pp. 389–393, 1982.
- [50] A. R. Liddle, “An Introduction to cosmological inflation,” in *ICTP Summer School in High-Energy Physics and Cosmology*, pp. 260–295, 1 1999.
- [51] S. Tsujikawa, “Introductory review of cosmic inflation,” in *2nd Tah Poe School on Cosmology: Modern Cosmology*, 4 2003.
- [52] J. A. Vázquez, L. E. Padilla, and T. Matos, “Inflationary Cosmology: From Theory to Observations,” 10 2018.
- [53] A. Achúcarro *et al.*, “Inflation: Theory and Observations,” 3 2022.
- [54] S. Clesse, “An introduction to inflation after Planck: from theory to observations,” in *10th Modave Summer School in Mathematical Physics*, 1 2015.
- [55] E. W. Kolb and M. S. Turner, *The Early Universe*, vol. 69. 1990.

- [56] A. Kosowsky and M. S. Turner, “CBR anisotropy and the running of the scalar spectral index,” *Phys. Rev. D*, vol. 52, pp. R1739–R1743, 1995.
- [57] K. N. Abazajian *et al.*, “CMB-S4 Science Book, First Edition,” 10 2016.
- [58] K. Abazajian *et al.*, “CMB-S4 Science Case, Reference Design, and Project Plan,” 7 2019.
- [59] K. Abazajian *et al.*, “CMB-S4: Forecasting Constraints on Primordial Gravitational Waves,” *Astrophys. J.*, vol. 926, no. 1, p. 54, 2022.
- [60] S. Adachi *et al.*, “Improved upper limit on degree-scale CMB B-mode polarization power from the 670 square-degree POLARBEAR survey,” 3 2022.
- [61] P. A. R. Ade *et al.*, “Improved Constraints on Primordial Gravitational Waves using Planck, WMAP, and BICEP/Keck Observations through the 2018 Observing Season,” *Phys. Rev. Lett.*, vol. 127, no. 15, p. 151301, 2021.
- [62] M. Tristram *et al.*, “Planck constraints on the tensor-to-scalar ratio,” *Astron. Astrophys.*, vol. 647, p. A128, 2021.
- [63] P. A. R. Ade *et al.*, “A Constraint on Primordial B-modes from the First Flight of the Spider Balloon-borne Telescope,” *Astrophys. J.*, vol. 927, no. 2, p. 174, 2022.
- [64] J. T. Sayre, C. L. Reichardt, J. W. Henning, P. A. R. Ade, A. J. Anderson, J. E. Austermann, J. S. Avva, J. A. Beall, A. N. Bender, B. A. Benson, F. Bianchini, L. E. Bleem, J. E. Carlstrom, C. L. Chang, P. Chaubal, H. C. Chiang, R. Citron, C. Corbett Moran, T. M. Crawford, A. T. Crites, T. de Haan, M. A. Dobbs, W. Everett, J. Gallicchio, E. M. George, A. Gilbert, N. Gupta, N. W. Halverson, N. Harrington, G. C. Hilton, G. P. Holder, W. L. Holzapfel, J. D. Hrubes, N. Huang, J. Hubmayr, K. D. Irwin, L. Knox, A. T. Lee, D. Li, A. Lowitz, J. J. McMahon, S. S. Meyer, L. M. Mocuano, J. Montgomery, A. Nadolski, T. Natoli, J. P. Nibarger, G. Noble, V. Novosad, S. Padin, S. Patil, C. Pryke, J. E. Ruhl, B. R. Saliwanchik, K. K. Schaffer, C. Sievers, G. Smecher, A. A. Stark, C. Tucker, K. Vanderlinde, T. Veach, J. D. Vieira, G. Wang, N. Whitehorn, W. L. K. Wu,

- and V. Yefremenko, “Measurements of b -mode polarization of the cosmic microwave background from 500 square degrees of sptpol data,” *Phys. Rev. D*, vol. 101, p. 122003, Jun 2020.
- [65] A. Kusaka *et al.*, “Results from the Atacama B-mode Search (ABS) Experiment,” *JCAP*, vol. 09, p. 005, 2018.
- [66] U. Seljak and M. Zaldarriaga, “Signature of gravity waves in polarization of the microwave background,” *Phys. Rev. Lett.*, vol. 78, pp. 2054–2057, 1997.
- [67] W. Hu and M. J. White, “A CMB polarization primer,” *New Astron.*, vol. 2, p. 323, 1997.
- [68] M. Kamionkowski and A. Kosowsky, “Detectability of inflationary gravitational waves with microwave background polarization,” *Phys. Rev. D*, vol. 57, pp. 685–691, 1998.
- [69] J. Martin, C. Ringeval, and V. Vennin, “Encyclopædia Inflationaris,” *Phys. Dark Univ.*, vol. 5-6, pp. 75–235, 2014.
- [70] Y. Akrami *et al.*, “Planck 2018 results. X. Constraints on inflation,” *Astron. Astrophys.*, vol. 641, p. A10, 2020.
- [71] W. T. Hu, “Wandering in the Background: A CMB Explorer,” other thesis, 8 1995.
- [72] J. Chluba and R. A. Sunyaev, “The evolution of CMB spectral distortions in the early Universe,” *Mon. Not. Roy. Astron. Soc.*, vol. 419, pp. 1294–1314, 2012.
- [73] J. Chluba, A. L. Erickcek, and I. Ben-Dayan, “Probing the inflaton: Small-scale power spectrum constraints from measurements of the CMB energy spectrum,” *Astrophys. J.*, vol. 758, p. 76, 2012.
- [74] J. Chluba, “Future Steps in CMB Cosmology,” in *53rd Rencontres de Moriond on QCD and High Energy Interactions*, pp. 337–356, 2018.
- [75] J. Chluba and R. A. Sunyaev, “Evolution of low-frequency features in the CMB spectrum due to stimulated Compton scattering and Doppler-broadening,” *Astron. Astrophys.*, vol. 488, p. 861, 2008.

- [76] J. Chluba, “Spectral distortions of the cosmic microwave background,” Juli 2005.
- [77] H. Tashiro, “CMB spectral distortions and energy release in the early universe,” *PTEP*, vol. 2014, no. 6, p. 06B107, 2014.
- [78] G. Giudice and R. Rattazzi, “Theories with gauge mediated supersymmetry breaking,” *Phys. Rept.*, vol. 322, pp. 419–499, 1999.
- [79] E. Silverstein and A. Westphal, “Monodromy in the CMB: Gravity Waves and String Inflation,” *Phys. Rev. D*, vol. 78, p. 106003, 2008.
- [80] L. McAllister, E. Silverstein, and A. Westphal, “Gravity Waves and Linear Inflation from Axion Monodromy,” *Phys. Rev. D*, vol. 82, p. 046003, 2010.
- [81] P. Svrček and E. Witten, “Axions In String Theory,” *JHEP*, vol. 06, p. 051, 2006.
- [82] C. Pahud, M. Kamionkowski, and A. R. Liddle, “Oscillations in the inflaton potential?,” *Phys. Rev. D*, vol. 79, p. 083503, 2009.
- [83] R. Flauger, L. McAllister, E. Pajer, A. Westphal, and G. Xu, “Oscillations in the CMB from Axion Monodromy Inflation,” *JCAP*, vol. 06, p. 009, 2010.
- [84] N. Kaloper and L. Sorbo, “A Natural Framework for Chaotic Inflation,” *Phys. Rev. Lett.*, vol. 102, p. 121301, 2009.
- [85] L. McAllister, E. Silverstein, A. Westphal, and T. Wrase, “The Powers of Monodromy,” *JHEP*, vol. 09, p. 123, 2014.
- [86] R. Easther and R. Flauger, “Planck Constraints on Monodromy Inflation,” *JCAP*, vol. 02, p. 037, 2014.
- [87] R. Flauger, L. McAllister, E. Silverstein, and A. Westphal, “Drifting Oscillations in Axion Monodromy,” *JCAP*, vol. 10, p. 055, 2017.
- [88] R. Flauger and E. Pajer, “Resonant Non-Gaussianity,” *JCAP*, vol. 01, p. 017, 2011.
- [89] N. K. Stein and W. H. Kinney, “Natural inflation after Planck 2018,” *JCAP*, vol. 01, no. 01, p. 022, 2022.

Appendices

A.1 The visible function $\mathcal{J}_\mu(z)$ and $\mathcal{J}_y(z)$

The visible function utilized in our SD calculation is gotten as the best-fitting approximation to the distortion Green's function using only μ and y distortion, and was taken from eq.(11a) and eq.(11b) in work [16]. The shape of visible functions in the redshift range $2 \times 10^6 \lesssim z \lesssim 10^3$ are shown in figure 3. The approximation of visible function assume that the transition between μ and y distortions is not abrupt at $z \approx z_\mu$.

$$\mathcal{J}_\mu(z) = \exp\left(-\left[\frac{z}{z_{\text{th}}}\right]^{5/2}\right) \left[1 - \exp\left(-\left[\frac{1+z}{1+z_{\mu y}}\right]^{1.88}\right)\right], \quad (1a)$$

$$\mathcal{J}_y(z) = \left[1 + \left(\frac{1+z}{6 \times 10^4}\right)^{2.58}\right]^{-1}. \quad (1b)$$

Where $z_{\mu,y} \approx 5 \times 10^4$ and $z_{\text{th}} \approx 1.98 \times 10^6$

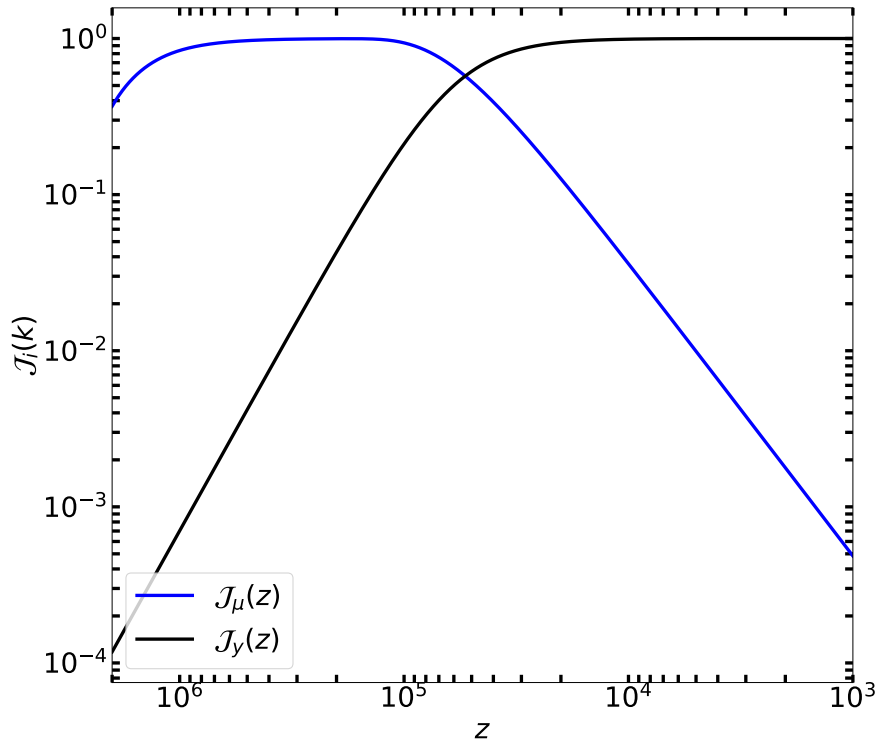


Figure 1: The visible function for μ and y SD in the redshift range $2 \times 10^6 \lesssim z \lesssim 10^3$.

B.2 Analytic exact form of δn_s

The equation used in section 5.3 for δn_s is an approximation from an exact expression that is established in eq.(3.25) in work [83], and has been plotted for $p_f = 1$ in figure 2 (red curve) in the range $10^{-5} \lesssim f_0 \lesssim 10^{-1}$. The eq.(2) is valid for $p_f = 1$ to first order in b and assumes the slow roll condition.

$$\delta n_s = \frac{12b}{\sqrt{1 + (3f_0\phi_*)^2}} \sqrt{\frac{\pi}{8} \coth\left(\frac{\pi}{2f_0\phi_*}\right)} f_0\phi_* \quad (2)$$

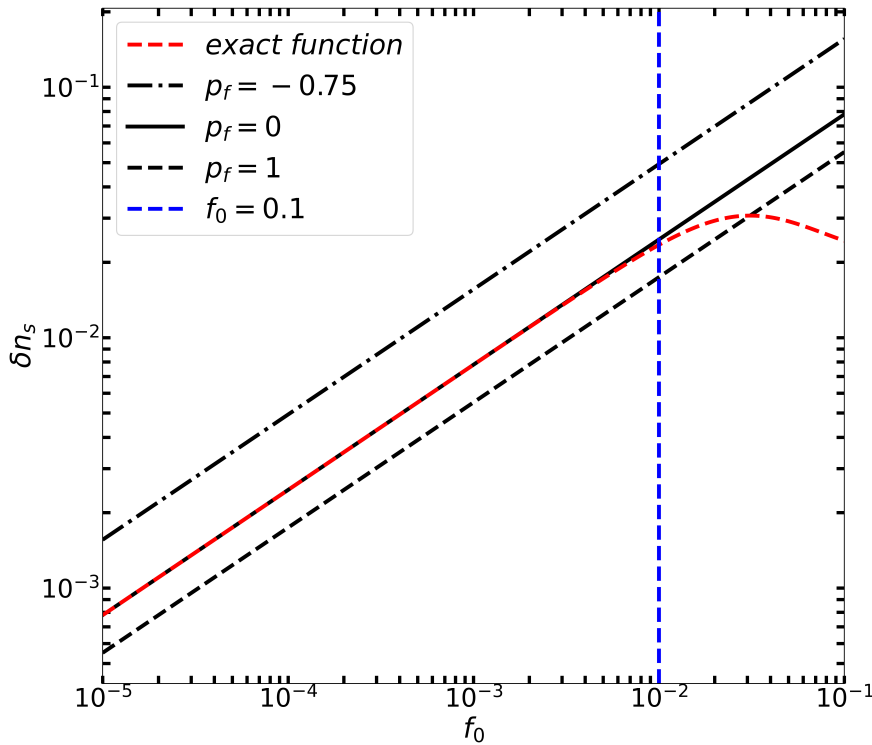


Figure 2: The approximations (black curves) and exact analytic (red curve) shape for δn_s are compared in the range $10^{-5} \lesssim f_0 \lesssim 10^{-1}$ for $p_f = 1$, black curves were plotted with eq.(5.7) for $p_f = \{-0.75, 0, 1\}$. The blue line shows the limit at which the approximation ceases to be good $f_0 \approx 1$.

C.3 The k -space window

The k -space window reduces the problem to a one-dimensional integral over k -space window functions for the effective μ and y distortions. The approximations $W^i(k)$ (where $i \in \{y, \mu\}$) are for the concordance cosmology, and were taken from eq.(24a) and eq.(24b) of work [28]. The shape of the k -space window in the wave number range $10^{-2} \lesssim k \lesssim 10^4$ are shown in figure 3, and mathematically is given by

$$W^y(k) \approx \frac{C^2}{2} e^{-2k^2/k_D^2(z_{\mu,y})}, \quad (3a)$$

$$W^\mu(k) \approx 2.8C^2 \exp\left(-\frac{\left[\frac{\hat{k}}{1360}\right]^2}{1 + \left[\frac{\hat{k}}{260}\right]^{0.3} + \left[\frac{\hat{k}}{340}\right]}\right) - 5.6W^y(k). \quad (3b)$$

Here $z_{\mu,y} \approx 5 \times 10^4$ and $\hat{k} := k/k_{\min}$ as the dimensionless momentum.

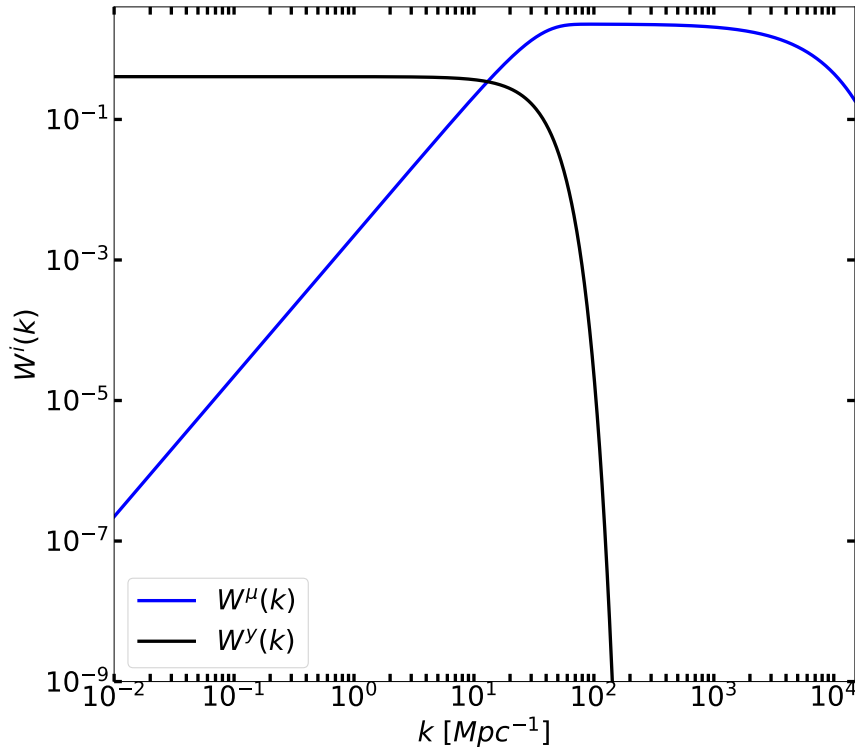


Figure 3: The k -space window function for μ and y SD plotted from eq.(3) in the wave number range $10^{-2} \lesssim k \lesssim 10^4$.